HARMONIA
International network for harmonization of atmospheric aerosol retrievals from ground based photometers

HARMONIA CA21119

Deliverable 2.4

Report on uncertainties for optimized and homogenized products and suggestions for improving already existing products

WG2 leaders: M. Campanelli, V. Estellés

Contributors: G. Kumar, M. García-Suñer, K. Chargazia, A. El Shahat

Date *23 October* 2026

cost EUROPEAN COOPERATION IN SCIENCE & TECHNOLOGY

Funded by the European Union

Introduction

1. The optimized Improved Langley Plot calibration method (ILPU) and uncertainty estimation.

2. Uncertainty assessment of the aerosol inversion products in SKYNET

3. Comparison of the aerosol size distributions obtained with AERONET, SKYNET and GRASP algorithms in the frame of the SAVEX-D campaign

4. Initial evaluation of photometer radiance and normalized radiance measurements in the NIR region (1627 nm and 2200 nm for PREDE-POM)

5. Calibration of Near-Infrared Channels of PREDE-POM Sun Photometers Using Standard and on Site Langley Plot Methods.

6. HARMONIA activity for the ESA Validation Center (EVDC)

Introduction

There is increasing evidence that the current earth system warming is mainly caused by anthropogenic emissions of greenhouse effect gases (such as carbon dioxide and methane). In this scenario, atmospheric aerosols contribute to the energy budget by reflecting back part of the solar radiation reaching the earth, with a net cooling effect. However, it is still challenging to estimate the contribution of the aerosols in the global budget. It is critical to improve our knowledge on the aerosol radiative properties, mainly at a global scale, because they are complex and very variable in space and time.

Aerosol properties such as Aerosol Optical Depth (AOD), Single Scattering Albedo (SSA), refractive index and size distributions are the most important variables describing the aerosols, typically used to represent the absorption and scattering properties. These variables are derived for the whole atmospheric column, by using sky and sun radiation measurements obtained with automatic state-of-the-art radiometers, available at an increasing number of ground level sites.

There are a few types of commercially available sun-sky radiometers, such as CIMEL CE318, PFR and PREDE POM. These instruments are, in turn, the standard instruments adopted by the international networks AERONET, GAW-PFR and SKYNET. Other types of low cost instruments are also available, although they are not usually organised in international networks. The advantages of the international networks are product homogeneity, traceability of calibration, quality assurance processes and centralised and user friendly access to the retrievals.

However, there exist differences between the approaches used by the different international networks that make the combined analysis challenging. In this sense, the main objective of the HARMONIA COST action was to work towards the products homogenization and harmonization, the improvement of the techniques used, and the synergy with other complementary techniques such as new low-cost instrumentation. In this frame, Working Group 2 was focused on the improvement of aerosol products. In particular, Deliverable 2.4 has been devoted to the estimation of uncertainties on aerosol products from optimized methods, with suggestions on future improvements.

The report is structured as follows: first, a new optimized method of calibration for sky radiometers is described (section 1) followed by the estimation and discussion of the uncertainties involved in both calibration and inversion steps (section 2). Section 3 is devoted to the validation of these new calibration and retrieval methods, by comparison with complementary measurements from aircraft during short campaigns. Next, sections 4 and 5 describe preliminary results on the calibration and of two new channels from the Prede POM02 radiometer, located in the longer wave band. And finally, section 6 describes the HARMONIA contribution to the provision of aerosol data for satellite cal/val activities, specifically in the ESA Cal/Val center (EVDC).

1. The optimized Improved Langley Plot calibration method (ILPU) and uncertainty estimation.

1.1 Introduction

The Improved Langley Plot (ILP) technique was developed by Campanelli et al. (2004), based on the previous study by Tanaka et al. (1986) and Nakajima et al. (1996). The purpose of developing the ILP technique was to regularly calibrate onsite the PREDE POM 1/2 skyradiometer, enabling regular monitoring of calibration values. At the same time, it removed the need to transport the instruments to a high-altitude site to perform a standard Langley plot (SLP) or to other lower level sites for calibration transfer. Unlike SLP, which can only be performed in a pristine environment with a stable atmosphere, ILP can be performed at a sea level site with variable aerosol loading. It is achieved by fitting the product of airmass, single scattering albedo (SSA) and scattering aerosol optical depth (AOD) with the logarithm of direct sun measurements, where the resulting intercept on the y-axis provides calibration values. However, the information about the scattering AOD and SSA is not available. Thus, diffused sky radiance measurements are used to retrieve the scattering AOD and derive SSA using the Skyrad 4.2 inversion algorithm. The ILP has proven to be one of the most robust methods to obtain the radiometric calibration values for decades, providing accurate calibration values within an uncertainty of 0.3 - 2.5% (depending on wavelength and site) (Campanelli et al., 2004; Uchiyama et al., 2018; Nakajima et al., 2020). However, recent studies by Campanelli et al. (2024) and Karanikolas et al. (2024) reported slight underestimation and discrepancies in the ILP calibration values. These discrepancies have highlighted the current need to further improve and reassess the methodological framework used in ILP.

After the inception of ILP by Campanelli et al. (2004) there has been little effort to update the ILP and, despite the subsequent development of Skyrad MRI v1 (Kobayashi et al., 2006), Skyrad 5 (Hashimoto et al., 2012), and Skyrad MRI v2 (Kudo et al., 2021), ILP still used the legacy inversion algorithm Skyrad 4.2. Campanelli et al. (2024) already recommended using the latest Skyrad MRI v2 in ILP. Following this recommendation, the present study develops an updated version of ILP by replacing the legacy Skyrad 4.2 with the latest Skyrad MRI v2. A key advantage of using the Skyrad MRI v2 is the updated optimisation method, where the retrieved products such as scattering and extinction AODs are constrained to the transmittance instead of direct AOD in Skyrad 4.2. This provides flexibility to the inversion process, where retrieved scattering and extinction are allowed to evolve freely during the inversion process. Based on this capability, we also develop an iteration-based scheme to obtain the monthly mean calibration value, as recommended by Tonna et al. (1995). We term this new method ILPU (Improved Langley Plot - Updated) and use it throughout the study.

In this report, we will first present the dataset used and the workflow of the ILPU method. The performance of the ILPU is assessed through convergence tests, followed by intercomparison of calibration values and AOD with reference networks.

1.2 Datasets

In this study, we used the data from the QUATRAM II and III campaigns in Rome (Italy) and Burjassot (Spain), corresponding to two European permanent SKYNET sites. QUATRAM II data covered May to September 2019, while QUATRAM III was conducted in September 2021. The campaign dataset includes data from two PREDE POM skyradiometers operated by the University of Valencia (POM-UV) and ISAC-CNR (POM-CNR), together with co-located PFR and CIMEL skyradiometers. At Burjassot, one year of measurement data from PREDE POM-02 spanning January to December 2023 was also used. Simultaneous AERONET version 3 level 2 direct data was also used for the comparison.

1.3 Working of ILPU

The workflow of the ILPU is presented in Figure 1.3.1. The red and blue regions represent the ILP and ILPU methods. In both methods, normalized radiance is used to retrieve the volume size distribution (VSD), while keeping the ground albedo, real and imaginary refractive index fixed at 0.1, 1.5 and 0.005 respectively. The only difference between the two methods is the use of the inversion algorithm: ILP uses Skyrad 4.2, while ILPU uses Skyrad MRI v2.

After retrieving the scattering AOD, the monthly mean calibration value is calculated using the method developed by Campanelli et al. (2004) in both ILP and ILPU. However, in the case of ILP (red region), this monthly mean calibration value is the final output, whereas in ILPU (blue region), this monthly mean calibration value acts as an initial guess, where it is used to calculate direct AOD and given as input to Skyrad MRI v2 for constraining the retrieval. The whole process is repeated again to calculate the monthly mean calibration value.

1.4 Convergence test

In the previous section, we explained the workflow of the ILPU and mentioned that the iteration process can be performed multiple times. One of the important aspects of this iterative procedure is to assess whether the calibration value remains stable and converges with increasing iterations or not. Therefore, we performed a convergence test where we performed 15 iterations from two different initial guesses in two rounds (Round A and Round B) to check stability and convergence. We used the POM-CNR data from the QUATRAM III campaign for this analysis.

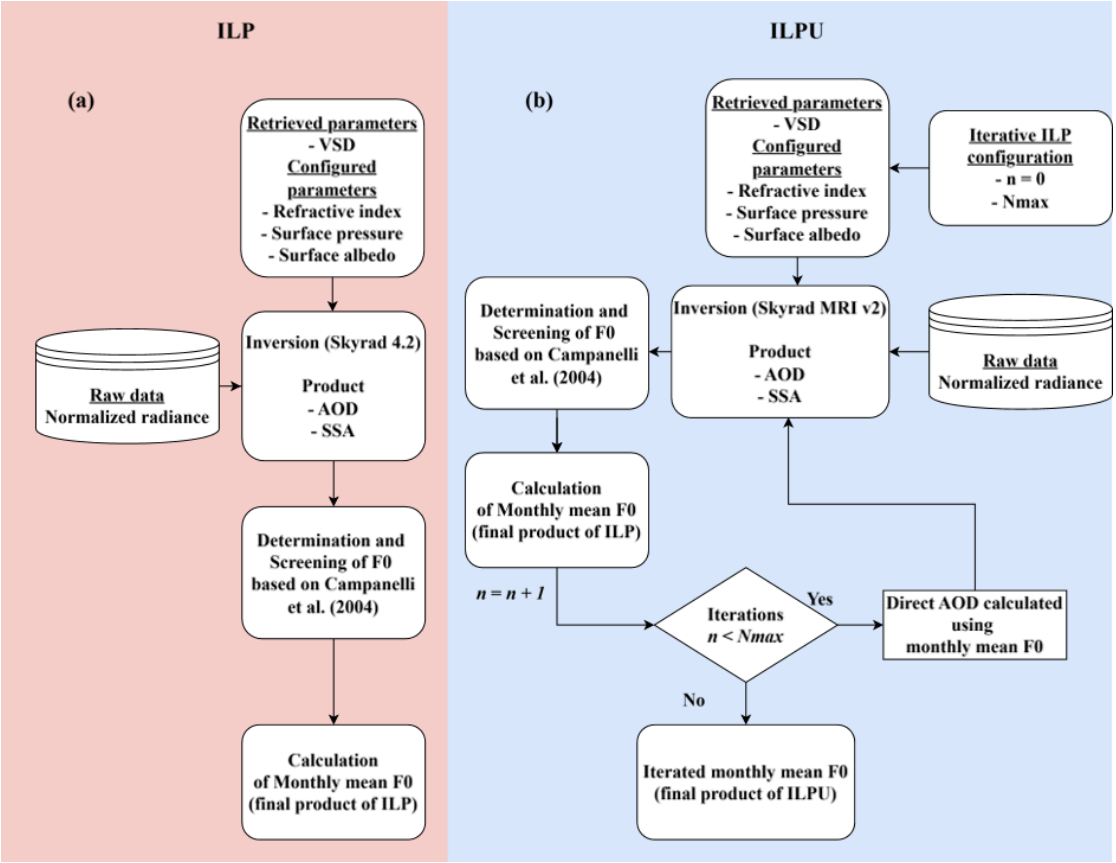


Figure 1.3.1- Workflow of ILP (Red) and ILPU (blue) calibration method

The first initial guess in Round A for this test was simply the first guess of the ILPU, while for the second initial guess for Round B, we simply increased the first initial guess by 3%. The value 3% was chosen arbitrarily, because convergence should not depend on the initial guess, but still it is a value higher than the expected uncertainty.

As we can see from the figure, irrespective of the first guess, the calibration values in the two rounds stabilised and converged within 15 iterations. The difference between the Round A and B calibration values after a single iteration fell from 3% to less than 0.4% for wavelengths greater than 400 nm, and 1.4 % at the 400 nm channel. Further iterations reduced the discrepancy to either 0 or less than 0.08%. For 340 nm, the stabilisation and convergence were slower, and it took 15 iterations for stabilisation in both rounds. Finally, the difference in the calibration values in the two rounds remained below 0.24%.

After the convergence test, we decided to use a single iteration in ILPU in the entire study. The choice of a single iteration is made to balance between convergence and computational time, since the majority of the discrepancy is removed in the single iteration for wavelengths above 340 nm, while additional iterations require several hours of computation. However, this is not a

recommendation, and the number of iterations must be decided based on future analysis done at sites with different characteristics.

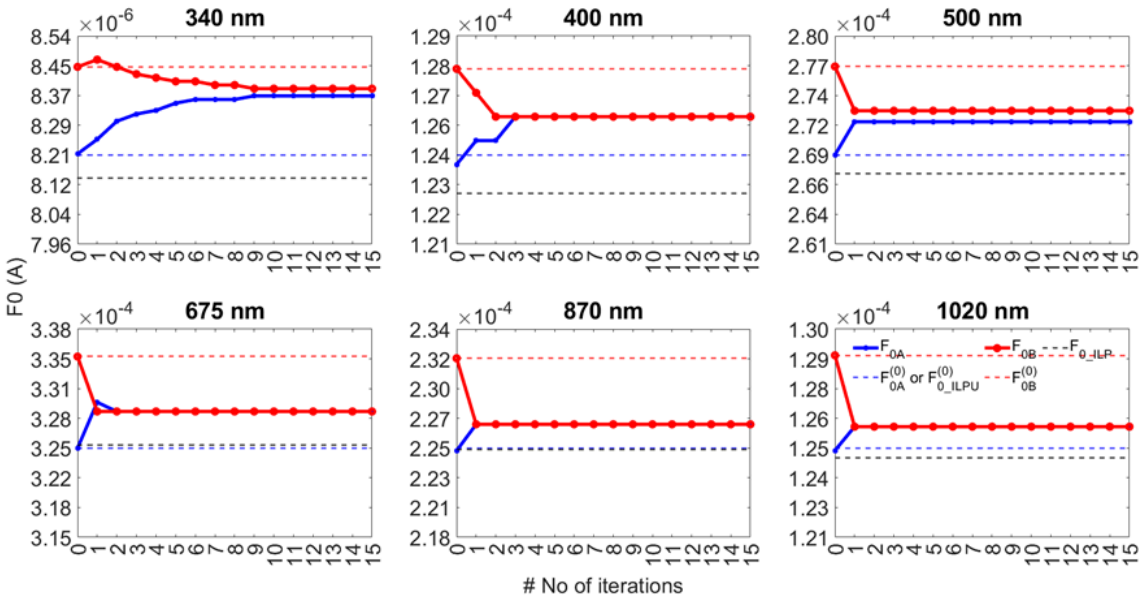


Figure 1.4.1- Convergence of ILPU calibration values across fifteen iterations across six wavelengths. The y-axis indicates the calibration value. The x-axis indicates the number of iterations.

1.5 Comparison of ILP, ILPU and calibration transfer from PFR and CIMEL during QUATRAM III campaign

Tables 1.1 and 1.2 summarise the comparison of ILP, ILPU and calibration transfer from PFR and CIMEL instruments during the QUATRAM III campaign for POM-UV and POM-CNR. The difference between the calibration values is calculated, considering the ILP and ILPU calibration values as a reference in Tables 1.1 and 1.2. As we can see, the ILPU calibration value reduces the discrepancy with CIMEL and PFR transfer calibration by 0.49 % to 1.3 % at all wavelengths except 1020 nm. At 1020 nm, the discrepancy with CIMEL increased by 0.55 % and 0.65 % for POM-UV and POM-CNR instruments. The increase in discrepancy at 1020 nm could be associated with temperature effects of one or both instruments; however, a detailed study is required to understand the exact cause of this discrepancy.

Table 1.5.1- Comparison of ILP and calibration transfer from PFR and CIMEL during QUATRAM III campaign

Method	340 nm	400 nm	500 nm	675 nm	870 nm	1020 nm
	POM-CNR					
PFR (transfer)	-	-	-2.53	-	-2.31	-
CE #1270 (transfer)	-3.91	-	-3.13	-1.29	-1.33	0.80
	POM-UV					
PFR (transfer)	-	-	-3.16	-	-2.07	-
CE #1270 (transfer)	-5.08	-	-3.16	-1.21	-1.94	2.39

Table 1.5.2- Comparison of ILPU and calibration transfer from PFR and CIMEL during QUATRAM III campaign

Method	340 nm	400 nm	500 nm	675 nm	870 nm	1020 nm
	POM-CNR					
PFR (transfer)	-	-	-1.21	-	-1.32	-
CE #1270 (transfer)	-2.96	-	-1.77	-0.45	-0.35	1.45
	POM-UV					
PFR (transfer)	-	-	-1.87	-	-1.58	-
CE #1270 (transfer)	-3.94	-	-1.87	-0.55	-1.45	2.94

1.6 Comparison of direct AOD during QUATRAM II and III campaigns

In this section, we will present the comparison of direct AOD using ILP and ILPU calibration values during QUATRAM II and QUATRAM III campaigns for POM-CNR. The PFR direct AOD and POM-CNR direct AOD processed using ILP calibration values were obtained from Karanikolas et al. (2024) while POM-CNR raw data were reprocessed using the ILPU calibration values with SUNRAD, which is a direct AOD retrieval algorithm used to retrieve direct AOD in SKYNET.

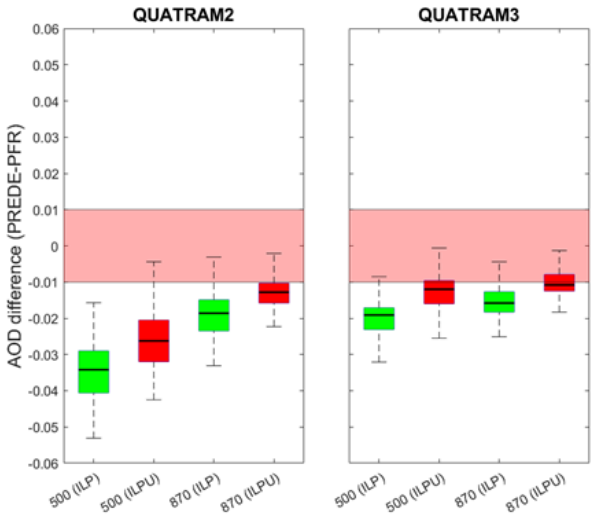


Figure 1.6.1- Box plot of the direct extinction AOD differences for POM CNR and PFR in QUATRAM II and III campaigns at 500 and 870 nm.

Figure 1.6.1 shows the box plot of the AOD difference between PFR and POM-CNR direct AOD at two common wavelengths of 500 and 870 nm. The pink band shows the AOD difference of ± 0.01. The green and red boxes refer to the distribution of AOD differences using ILP and ILPU calibration values. The black line within the red and green boxes shows the median AOD difference.

The median AOD difference has decreased for both wavelengths using ILPU calibration. Karanikolas et al. (2024) reported that the PFR-PREDE AOD differences were generally outside the ±0.01 range and identified a systematic underestimation of the ILP calibration values as one of the causes. In the present analysis using ILPU calibration values, the shift of the median AOD difference towards the pink band indicates that ILPU has reduced the reported underestimation.

We also calculated the number of points within the WMO limit, defined as ±(0.005 + 0.01/m), where the airmass. Table 1.6.1 shows the fraction of points within the WMO limit during the

QUATRAM II and III campaigns using ILP and ILPU calibration values. During QUATRAM II, the fraction of points increased from 0 to 2.5 % and from 11.7% to 41% at 500 and 870 nm, respectively. During QUATRAM III, the fraction of points increased from 2.3 to 43.5% and from 14.7% to 58.5% at 500 and 870 nm, respectively. Although at least 95% of the points have to be within the WMO limit, the substantial increase in the fraction of points demonstrates the improvement in the ILPU calibration values.

Table 1.6.1- Statistics of fraction of points within the WMO limit during QUATRAM II and III campaigns using ILP and ILPU.

Campaign	Year		No of data points	Points within WMO limit (%) *(ILP)*		Points within WMO limit (%) (ILPU)	
				500 nm	870 nm	500 nm	870 nm
QUATRAM II	2019	5 months	3806	0	11.7	2.5	41
QUATRAM III	2021	1 month	1221	2.3	14.7	43.5	58.5

1.7 Comparison of direct AOD at Burjassot site

To evaluate the performance of the ILPU over a longer period, one year of data from January to December 2023 at the permanent Burjassot station was analyzed. The direct data were processed using both ILP and ILPU calibration values and compared with simultaneous AERONET version 3 level 2 direct AOD from the co-located CIMEL radiometer. Data with a maximum temporal gap of 10 s at common wavelengths of 340, 380, 500, 675, 870 and 1020 were selected for this analysis. To assess the performance of the ILPU, we repeated the analysis from the previous section and plotted a box plot of the AERONET-PREDE AOD difference and calculated the fraction of data points within the WMO limit.

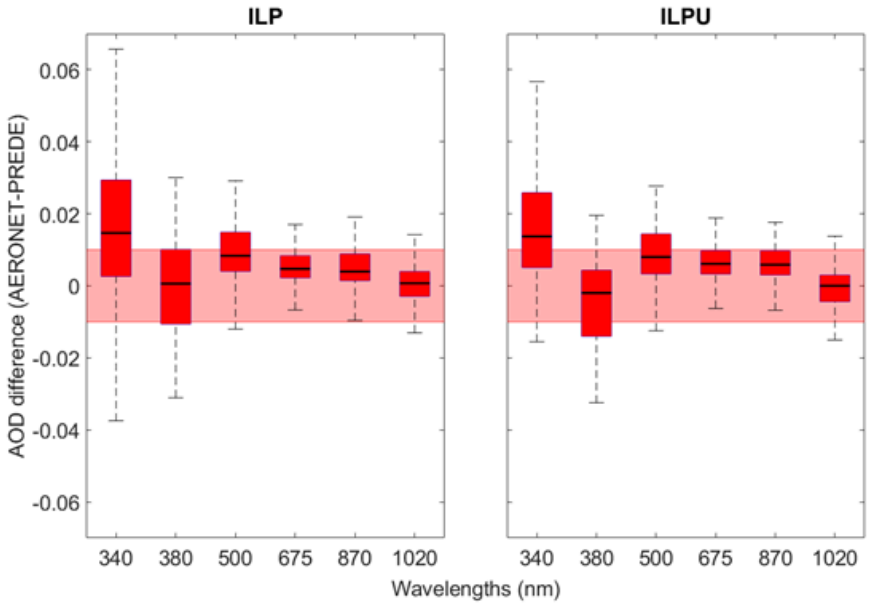


Figure 1.7.1- Box plot of the direct extinction AOD differences for PREDE-POM and AERONET in the Burjassot site (València) for ILP (left) and ILPU (right).

Table 1.7.1-Statistics of fraction of points within the WMO limit at Burjassot site in Valencia using ILP and ILPU.

Wavelength	No of data points	Points within WMO limit (%) (ILP)	Points within WMO limit (%) (ILPU)
340	788	26	40
380	788	51	64
500	788	64	66
675	788	88	82
870	788	91	89
1020	787	90	89

Unlike the results from the QUATRAM II and III campaigns, the improvements here are limited. The median AOD difference falls within the pink band at all wavelengths except 340 nm. However, using the ILPU slightly reduces the median difference. To quantify whether this reduction in the median difference also translates into improved agreement with the reference instrument, we examined the fraction of points within the WMO limits. Table 1.7.1 presents the fraction of points within the WMO limits using ILP and ILPU. We can see that the points within the WMO limits increased from 26 to 40 %, 51 to 64 % and 64 to 66% at 340, 380 and 500 nm. However, the fraction of points decreased from 88 to 82 %, 91 to 89% and 90 to 89% at 675, 870 and 1020 nm, respectively. This clearly shows the improvement due to ILPU, largely visible at shorter wavelengths, while no improvement is observed at the longer wavelengths.

1.8 Uncertainty assessment of the ILPU method

The uncertainty of the calibration value is one of the most important parameters in the evaluation of the reliability of the calibration method. Since the calibration value directly affects the retrieval of the direct products and indirectly affects the inversion aerosol products, uncertainty associated with the calibration value also propagates to the final aerosol products. In the case of ILP, there have been studies that reported its uncertainty, which varied from 0.3 to 2.5 % depending on the wavelength and site. ILPU is a new method, and to determine its reliability, it is important to quantify its uncertainty. In this study, we will estimate the uncertainty of the ILPU following the method described by Nakajima et al. (2020) using QUATRAM III data for POM-CNR and POM-UV.

The method used by Nakajima et al (2020) is based on the error propagation method, where the error associated with every component in the equation used for the ILP is propagated to compute the final ILP calibration uncertainty. In ILPU, we also use the same equation as the ILP; we can also calculate the uncertainty using the same method.

The equation used for the regression in ILP is written as:

$$y = a + bx + u$$

where , $y = ln(F)$ and F is the direct sun data, $a = F_0$, F_0 is the calibration value, $b = \frac{-1}{\omega}$, and $x = m\tau_{sca} = m\omega\tau$, being m the airmass, ω is SSA, τ_{sca} is scattering AOD, and τ is extinction AOD, and u is the residual.

Assuming x is the independent variable and it is related to y, including a random residual u, then the dispersion in x (it is, σ_x) can be written as,

$$\left(\frac{\sigma_x}{\bar{x}}\right)^2 \sim \frac{\sigma_{m0}^2}{\overline{m0}^2} + \frac{\sigma_\tau^2}{\bar{\tau}^2} + \frac{\sigma_\omega^2}{\bar{\omega}^2}$$

where, σ_{m0}, σ_τ and σ_ω are the dispersions of airmass, extinction AOD and SSA during ILPU.
Following Nakajima et al. (2020) the corresponding σ_{ILPU} can be written as:

$$\sigma_{ILPU} = 3.5\frac{\overline{m0}^2}{|m2-m1|}\gamma\bar{\tau},$$

where γ represent the retrieval error, m2 and m1 are the lower and upper limits of the airmass while m0 is the mean airmass. $\bar{\tau}$ is the monthly mean extinction AOD.

We found that m1 was 1.2 for QUATRAM III, whereas the upper limit of ILPU is m=3. The value of γ was assumed to be 15% (Nakajima et al., 2020). Finally, we calculated the monthly mean uncertainty of the ILPU using one iteration in Table 1.8.2.

Table 1.8.1- Monthly mean uncertainty of ILPU using POM-UV and CNR during QUATRAM III campaign

(%)	340	400	500	675	870	1020
POM-CNR	1.70	1.40	1.03	0.66	0.43	0.37
POM-UV	1.72	1.43	1.06	0.67	0.46	0.37

The monthly mean uncertainty of the ILPU method, including one iteration, varied from 0.37% to 1.72% for both POM-UV and POM-CNR instruments. The monthly mean uncertainty is consistent across both instruments, and it also lies within the uncertainty range of ILP, which ranges from 0.3 to 2.5% reported by Campanelli et al. (2004), Uchiyama et al. (2018) and Nakajima et al. (2020).

1.9 Suggestions for improvement

So far, we demonstrated that the ILPU can provide stable and more accurate calibration values than the previous ILP version. However, the improvements were mostly limited to the shorter wavelengths, particularly for wavelengths smaller than 675 nm. For wavelengths above 500 nm, the results did not improve and showed some discrepancy at 1020 nm. Future work should include more sites with different aerosol loading to confirm the universality of the improvements introduced. Also, to understand any systematic bias due to the algorithm, ILPU would be performed using other inversion algorithms such as GRASP.

References:

Campanelli, M., Estellés, V., Kumar, G., Nakajima, T., Momoi, M., Gröbner, J., Kazadzis, S., Kouremeti, N., Karanikolas, A., Barreto, A., Nevas, S., Schwind, K., Schneider, P., Harju, I., Kärhä, P., Diémoz, H., Kudo, R., Uchiyama, A., Yamazaki, A., Iannarelli, A. M., Mevi, G., Di Bernardino, A., and Casadio, S.: Evaluation of on-site calibration procedures for SKYNET Prede POM sun–sky photometers, Atmos. Meas. Tech., 17, 5029–5050, https://doi.org/10.5194/amt-17-5029-2024, 2024.

Campanelli, M., Nakajima, T., and Olivieri, B.: Determination of the solar calibration constant for a sun-sky radiometer: proposal of an in-situ procedure, Appl. Opt.,43, 651–659, https://doi.org/10.1364/AO.43.000651, 2004.

Hashimoto, M., Nakajima, T., Dubovik, O., Campanelli, M., Che, H., Khatri, P., Takamura, T., and Pandithurai, G.: Development of a new data-processing method for SKYNET sky radiometer observations, Atmos. Meas. Tech., 5, 2723–2737, https://doi.org/10.5194/amt-5-2723-2012, 2012.

Karanikolas, A., Kouremeti, N., Campanelli, M., Estellés, V., Momoi, M., Kumar, G., Nyeki, S., and Kazadzis, S.: Intercomparison of aerosol optical depth retrievals from GAW-PFR and SKYNET sun photometer networks and the effect of calibration, Atmos. Meas. Tech., 17, 6085–6105, https://doi.org/10.5194/amt-17-6085-2024, 2024.

Masayuki Tanaka, Teruyuki Nakajima, and Masataka Shiobara, "Calibration of a sunphotometer by simultaneous measurements of direct-solar and circumsolar radiations," Appl. Opt. 25, 1170-1176 (1986)

Nakajima, T., Campanelli, M., Che, H., Estellés, V., Irie, H., Kim, S. W., Kim, J., Liu, D., Nishizawa, T., Pandithurai, G., Kumar Soni, V., Thana, B., Tugjsurn, N. U., Aoki, K., Go, S., Hashimoto, M., Higurashi, A., Kazadzis, S., Khatri, P., Kouremeti, N., Kudo, R., Marenco, F., Momoi, M., Ningombam, S. S., Ryder, C. L., Uchiyama, A., and Yamazaki, A.: An overview of and issues with sky radiometer technology and SKYNET, https://doi.org/10.5194/amt-13-4195-2020, 10 August 2020.

Tonna, G., Nakajima, T., and Rao, R.: Aerosol features retrieved from solar aureole data: a simulation study concerning a turbid atmosphere, Appl Opt. 4486-99, doi: 10.1364/AO.34.004486, 1995.

Uchiyama, A., Matsunaga, T., and Yamazaki, A.: The instrument constant of sky radiometers (POM-02) – Part 1: Calibration constant, Atmos. Meas. Tech., 11, 5363–5388, https://doi.org/10.5194/amt-11-5363-2018, 2018

2. Uncertainty assessment of the aerosol inversion products in SKYNET

2.1 Introduction

Inversion aerosol products are often used in intercomparison between instruments and networks, aerosol climatology and studies of aerosol radiative effects. Differences observed in these applications can reflect real atmospheric variability, but some or all of the difference may arise from measurement errors, retrieval assumptions, or instrumental errors. Therefore, it is essential to evaluate the uncertainty and understand whether the observed differences are meaningful or are within the retrieval uncertainty.

In this study, we estimated the uncertainty of the retrieved aerosol products from Skyrad MRI v2. For this purpose, we used the method described by Sinyuk et al. (2020).

2.2 Datasets

For this study, we used data from two sites: BASS (Burjassot Atmospheric Station) in Burjassot, Valencia, Spain, covering 3-7 January and 1-5 August 2023, and the National Atmospheric Research Laboratory (NARL) site at Gadanki in Andhra Pradesh, India, covering March 2023.

We selected these two sites to represent a broad range of aerosol loading. The aerosol loading at BASS is relatively low, with a maximum AOD below 0.4, while the aerosol loading is higher in Gadanki, with AOD reaching as high as 1.6.

2.3 Methodology

To assess the uncertainty of the retrieved aerosol products from Skyrad MRI v2, we performed a perturbation analysis similar to the method described by Sinyukl et al. (2020). The three input parameters (radiometric calibration values, SVA and ground albedo) were perturbed using positive, zero and negative biases. The calibration values and the SVA were perturbed by ±2.5% and ±5%. Ground albedo was varied by +0.05, 0 and -0.02. As a result of this perturbation, we obtained 27 sets of retrieved aerosol products: real and imaginary refractive index and SSA. These products were then screened to contain only simultaneous measurements, and the standard deviation of each set of 27 retrievals was calculated to represent U27 uncertainty. Simultaneously, we processed the direct AOD using the SUNRAD code (Estellés et al., 2012). We then collocated the direct AOD within the 10-minute interval of the screened retrievals and binned the direct AOD at 400 nm in various bins such as 0-0.05, 0.05-0.1, 0.1-0.2, 0.2-0.4, with a 0.2 step up to 1.4. The U27 uncertainty corresponding to each retrieval was then binned into different bins. Finally, the U27 mean uncertainty was calculated as the average of the U27 uncertainty in each bin and a one-dimensional lookup table was created.

2.4 Results

Figures 2.4.1 and 2.4.2 represent the U27 mean uncertainty in SSA and refractive index as a function of direct AOD at 400 nm at the seven wavelengths from PREDE POM instruments (340, 380, 400, 500, 675, 870 and 1020 nm) at the BASS and NARL Gadanki. U27 mean uncertainty follows a power-law function and decreases with increasing AOD. For SSA, uncertainty decreases rapidly with increasing AOD at BASS, while the reduction is slow as AOD increases beyond 0.4 at NARL Gadanki. These results are consistent with the results produced by Sinyuk et al. (2020) in spite of using different algorithm implementations.

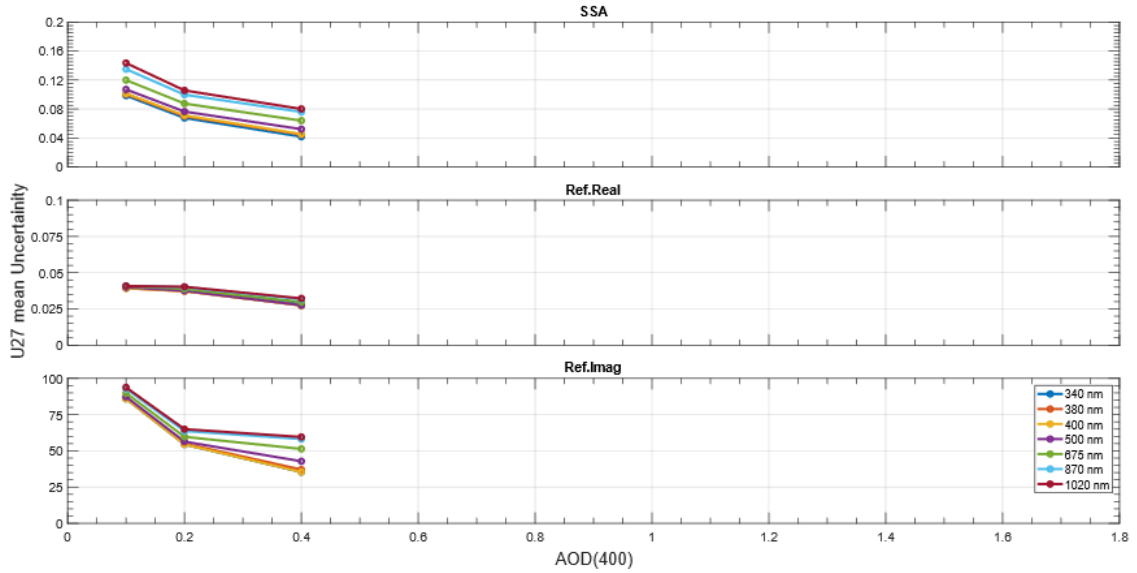


Figure 2.4.1-SSA, real and imaginary refractive index uncertainties for various AOD bins at Valencia.

The results for both real and imaginary refractive index are also consistent with Sinyuk et al. (2020). Similar to SSA, the refractive index follows the same behaviour, with uncertainty decreasing as AOD increases. The maximum uncertainty for the real and imaginary refractive index is approximately 0.04 and 100% for AOD < 0.2, respectively. For AOD above 1.4, the uncertainties decrease to below 0.01 and 60 % for the real and imaginary refractive indices. Although there is a temporary increase in the real and imaginary refractive indices in the AOD bins at 0.8 and 1.0, these could be related to the relatively small number of observations available in these bins.

Overall, the estimated uncertainty for SSA, real and imaginary refractive index for AOD above 0.2 is below 0.07, 0.04 and 75% for all the wavelengths. These results are also consistent with the uncertainty reported by Kudo et al. (2021) and Dubovik et al. (2000).

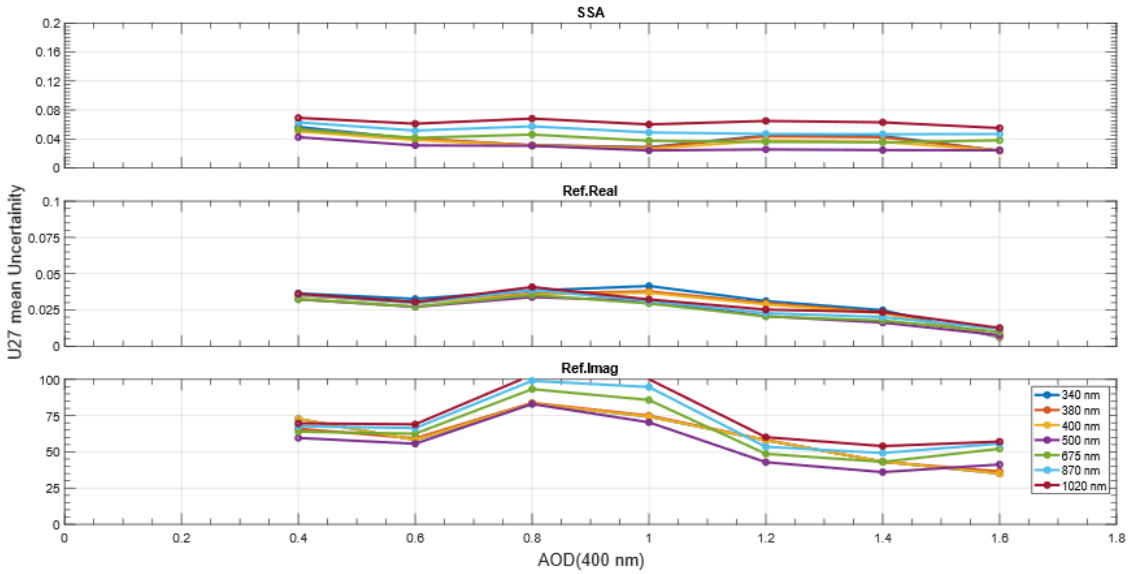


Figure 2.4.1-SSA, real and imaginary refractive index uncertainties for various AOD bins at Gadanki.

2.5 Suggestion for improvement

Future work should extend the uncertainty analysis to include sites with different characteristics and longer data durations. The large dataset should provide sufficient data to create a 3D lookup table using direct AOD at 400 nm, Ångström exponent at 400-875nm and SSA, similar to Sinyuk et al. (2020). This look-up table would provide an operational uncertainty estimate for the aerosol retrieval products using SKyrad MRI v2 within SKYNET.

References:

Dubovik, O., Smirnov, A., Holben, B. N., King, M. D., Kaufman, Y. J., Eck, T. F., & Slutsker, I. (2000). Accuracy assessments of aerosol optical properties retrieved from Aerosol Robotic Network (AERONET) Sun and sky radiance measurements. Journal of Geophysical Research: Atmospheres, 105(D8), 9791–9806. https://doi.org/https://doi.org/10.1029/2000JD900040

Kudo, R., Diémoz, H., Estellés, V., Campanelli, M., Momoi, M., Marenco, F., Ryder, C. L., Ijima, O., Uchiyama, A., Nakashima, K., Yamazaki, A., Nagasawa, R., Ohkawara, N., and Ishida, H.: Optimal use of the Prede POM sky radiometer for aerosol, water vapor, and ozone retrievals, Atmos. Meas. Tech., 14, 3395–3426, https://doi.org/10.5194/amt-14-3395-2021, 2021

Sinyuk, A., Holben, B. N., Eck, T. F., Giles, D. M., Slutsker, I., Korkin, S., Schafer, J. S., Smirnov, A., Sorokin, M., and Lyapustin, A.: The AERONET Version 3 aerosol retrieval algorithm, associated uncertainties and comparisons to Version 2, Atmos. Meas. Tech., 13, 3375–3411, https://doi.org/10.5194/amt-13-3375-2020, 2020.

3. Comparison of the aerosol size distributions obtained with AERONET, SKYNET and GRASP algorithms in the frame of the SAVEX-D campaign.

3.1 Introduction: The SAVEX-D campaign

The Sunphotometer Airborne Validation EXperiment in Dust (SAVEX-D) campaign was held at the Cape Verde archipelago in August 2015. The main objective of this experiment was to validate ground-based sun-photometer retrievals from the AERONET and the ESR/SKYNET networks with vertically-integrated in-situ airborne observations. This way, the discrepancies between the instruments and the inversion algorithms implemented by each network could be examined using as reference an independent dataset. The location of the archipelago near the Sahara desert, which is a source of dust particles, ensures good conditions for the inversion, with AOD ranging between 0.4 and 0.6.

Two flights were operated, as seen in Figure 3.1. The first was scheduled over Praia on 16 August from 14:45 to 19:01h. The flight planned on August 25, however, took off from Praia but had to be redirected to Sal island. The reason was the presence of clouds, which complicated aerosol measurements. The duration of this flight was less than the other, as the plane took off at 14:39 and landed at 18:00h. Given the difficulties experienced during the flight on August 25, the analysis presented in this report focuses exclusively on measurements from August 16.

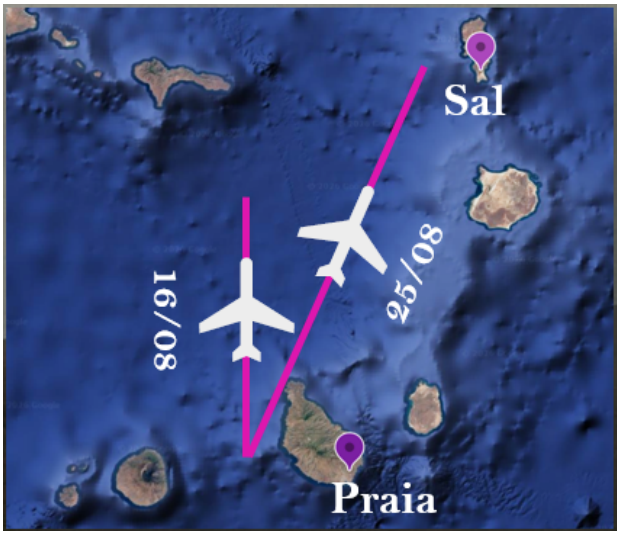


Figure 3.1. Map showing the location of Praia measurement station and Sal island along with the trajectories of the flights carried out during the SAVEX-D campaign. Figure done using *Google Earth*.

3.2 Instrumentation

As it has been mentioned, one of the particularities of the SAVEX-D campaign is that ground and in-situ based measurements were simultaneously performed over the same location (except on 25 August, as the plane flew towards Sal island, but the ground-based instrumentation was not displaced). This made possible the comparison of aerosol properties obtained from independent methodologies.

3.2.1. In-situ measurements

The in-situ equipment was installed aboard the BAe-146 aircraft operated by the Facility for Airborne Atmospheric Measurements (FAAM), with access provided through the European Facility for Airborne Research (EUFAR) (see Figure 3.2a). Given that the characterisation of the Volume Size Distribution was one of the main objectives of the campaign, different instruments were used to cover the maximum size interval (Figure 3.2b). In particular, Passive Cavity Aerosol Spectrometer Probes (PCASP) covered the range from $0.1 - 3\ \mu m$, Cloud Droplet Probes (CDP) took measurements from $2 - 50\ \mu m$ and Cloud Image Probes (CIP-15) could measure from $15 - 930\ \mu m$.



Figure 3.2. a) Bae-146 FAAM aircraft leaving for data acquisition. b) Detail of the aircraft, where the PCASP (white cylinder with the yellow label) and the CDP (over the PCASP) can be spotted.

3.2.2. Ground-based measurements

During the time period of the SAVEX-D campaign, a ground-based measurement station was conveniently installed at Praia's airport (Figure 3.3a). Here, the Cimel CE-318 from the Met Office (belonging to the AERONET network) collected data next to a Prede POM-01 from the University of València, belonging to the European SkyRad network (ESR/SKYNET). Figures 3.3b and 3.3c show these instruments, respectively. The AERONET and the SKYNET networks provide similar products based on solar/lunar direct and almucantar measurements despite using different instruments and processing algorithms. However, while AERONET is extended almost worldwide, sites participating in the SKYNET network are concentrated in Asia and part of Europe. Therefore, comparing the retrievals of the instruments from these two networks and assessing the differences between instrumentation and processing algorithms becomes a key task towards the harmonisation of photometric measurements. In addition, this would also help to understand the current limitations and issues related to this technique.





Figure 3.3. a) Ground-based measurement station located at Praia airport. The Prede can be spotted at the roof of the white container, while the Cimel can be seen on the left, set in a tripod. b) Closer look of the Cimel CE-318. c) Closer look of the Prede POM-01.

3.3 Inversion algorithms

In this analysis, the almucantar measurements of the Prede and Cimel photometers will be processed with different algorithms in order to compare the products obtained.

Thus, for the Cimel, the AERONET's V3 Level 1.5 retrievals will be considered. V3 constitutes the most up-to-date version of AERONET's processing algorithm (Sinyuk et al. 2020). The corresponding products can be downloaded from AERONET's website. Among the major improvements with respect to its predecessor, the V2, we can mention the better characterisation of NO_2 and H_20, and the implementation of the temperature correction for each wavelength (Giles et al. 2019), as well as the improvement in the characterisation of the bidirectional reflectance distribution function (BRDF) (Sinyuk et al. 2020).

Additionally, raw data from the Cimel will be adapted and processed with GRASP (Dubovik et al. 2014). This open source algorithm, based on AERONET's heritage, can be used to compute a large number of aerosol and surface properties. Indeed, it is being quite relevant for the aerosol retrieval community, as it is able to process measurements independently of the type of instrument: satellites, ground-based or airborne. Furthermore, not only its versatility has been praised, but also its successful performance when characterising bright surfaces such as deserts.

In the case of the Prede, almucantar measurements will be processed using several versions of the SKYRAD.pack algorithm to study the differences in their performance: Skyrad 4.2, Skyrad 5 and Skyrad MRI V2. The SKYRAD.pack was first developed by Nakajima et al. 1996 to

process data from Prede instruments. One of the most relevant versions of this algorithm is Skyrad 4.2. This procedure showed some room for improvement, as according to Hashimoto et al. 2012, it was prone to confound clouds with coarse particles. This led them to develop Skyrad 5, with an improved cloud screening routine and a method for smoothing the results by setting strong constraints to reduce size distribution at radii greater than $10\ \mu m$. The latest version of the SKYRAD algorithm, developed at the Meteorological Research Institute (MRI) of Japan, is Skyrad MRI v2 (Kudo et al. 2021). Among the improvements introduced, we can find the optimisation of the smoothness constraints that were introduced in Skyrad 5 as well as the implementation of different particle models, namely spheroid, voronoi and hexahedral.

On the other hand, analogously to the Cimel, the GRASP algorithm will be run based on the Prede measurements. This application becomes quite interesting, as it allows us to compare the retrievals from measurements corresponding to different instruments that have been processed by the same algorithm.

3.4 Intercomparison results

In this section, the main outcomes of the comparison of Prede and Cimel inversion products as well as with in-situ data are described. First, the choice in the set of calibration coefficients for the processing of Prede data using GRASP have been justified. Then, the SSA retrieved by the different algorithms is intercompared. Finally, the volume size distributions are compared with each other and with the in-situ data.

3.4.1. Choosing the best set of calibration coefficients for the Prede processing with GRASP

The Prede measurements from the SAVEX-D campaign were suitable to compute the calibration coefficients for the instrument using different methods and perform a small test on how these affect the results of the inversion. Hence, apart from the calibration coefficients provided by the International SKYNET Data Center (ISDC), the set of coefficients computed based on the Improved Langley Plot using MRI and the obtained from the Updated Improve Langley Plot method (UILP), from Kumar et al. 2026, have also been regarded.

The key question here is to find out what is the best choice for the calibration coefficients. Focusing on the data inversion using GRASP, the set of coefficients that leads to smaller residuals, i.e. smaller differences between the fit and measured radiances, will be implemented for data processing. Table 3.1 shows, for each calibration method, the three largest radiance differences along with the corresponding scattering angle. In particular, the values of the measured and fit radiances as well as their difference ($\Delta R = R_{meas} - R_{fit}$) are included. These results correspond to the 870 nm channel, the one that presents larger discrepancies between the computed and measured radiances. Figures 3.4 complement the results in Table 3.1. In particular, Figures 3.4a, c and e illustrate the differences in the

measured and fit radiances as a function of the scattering angle for the ISDC, ILP with MRI and UILP methods, respectively. The largest discrepancies can be spotted at the smallest scattering angles. On the other hand, Figures 3.4b, d and f show the scatter plot between the measured and the fit radiances for the ISDC, ILP with MRI and UILP methods, respectively. The dashed dark blue line represents the perfect agreement, while the linear regression for the data points is drawn in cyan. It is important to mention that, for the processing, only scattering angles in the range between 3.5º and 180º are considered. The effect of stray light becomes significant at scattering angles smaller than 3.5º. Therefore, although radiances at small scattering angles provide valuable information for the characterisation of the coarse mode, the large radiance residuals related to problems in the proper modelisation of this phenomenon force to drop these angles in the retrieval. Based on Table 3.1 and Figures 3.4, one could state that the set of calibration coefficients computed using the UILP seems to yield slightly better results than the other methods, so the GRASP inversion products from Prede that will be shown in this report are computed based on the UILP calibration coefficients. For future work, the Skyrad 4.2, 5 and MRI v2 can be reprocessed based on the UILP calibration. In this report, the retrievals for these algorithms are derived from ISDC's calibration. Nevertheless, given that the measured radiances obtained with the three calibrations differ by less than 1% (Table 3.1), the impact of this difference on the intercomparison is expected to be small.

Table 3.1. Values of the three largest differences between the measured and fit radiances with the corresponding scattering angles for the three sets of calibration coefficients computed for the Prede, at 870 nm. The radiance residuals have been defined as $\Delta R = R_{meas} - R_{fit}$*, with* R_{meas} *and* R_{fit} *the measured and fit radiances, respectively. The* ΔR *for the UILP have been highlighted because these are generally the smallest in comparison to the other methods.*

	ISDC			**ILP with MRI**			**UILP**		
Sca (º)	4.00	3.69	3.89	4.00	3.69	3.89	4.00	3.69	3.89
R_{meas}	11.40	5.73	4.53	11.38	5.72	4.53	11.30	5.68	4.49
R_{fit}	5.79	1.80	1.08	5.78	0.89	0.73	5.79	1.71	1.07
ΔR	**5.61**	**3.93**	**3.45**	**5.60**	**4.83**	**3.80**	**5.50**	**3.97**	**3.43**

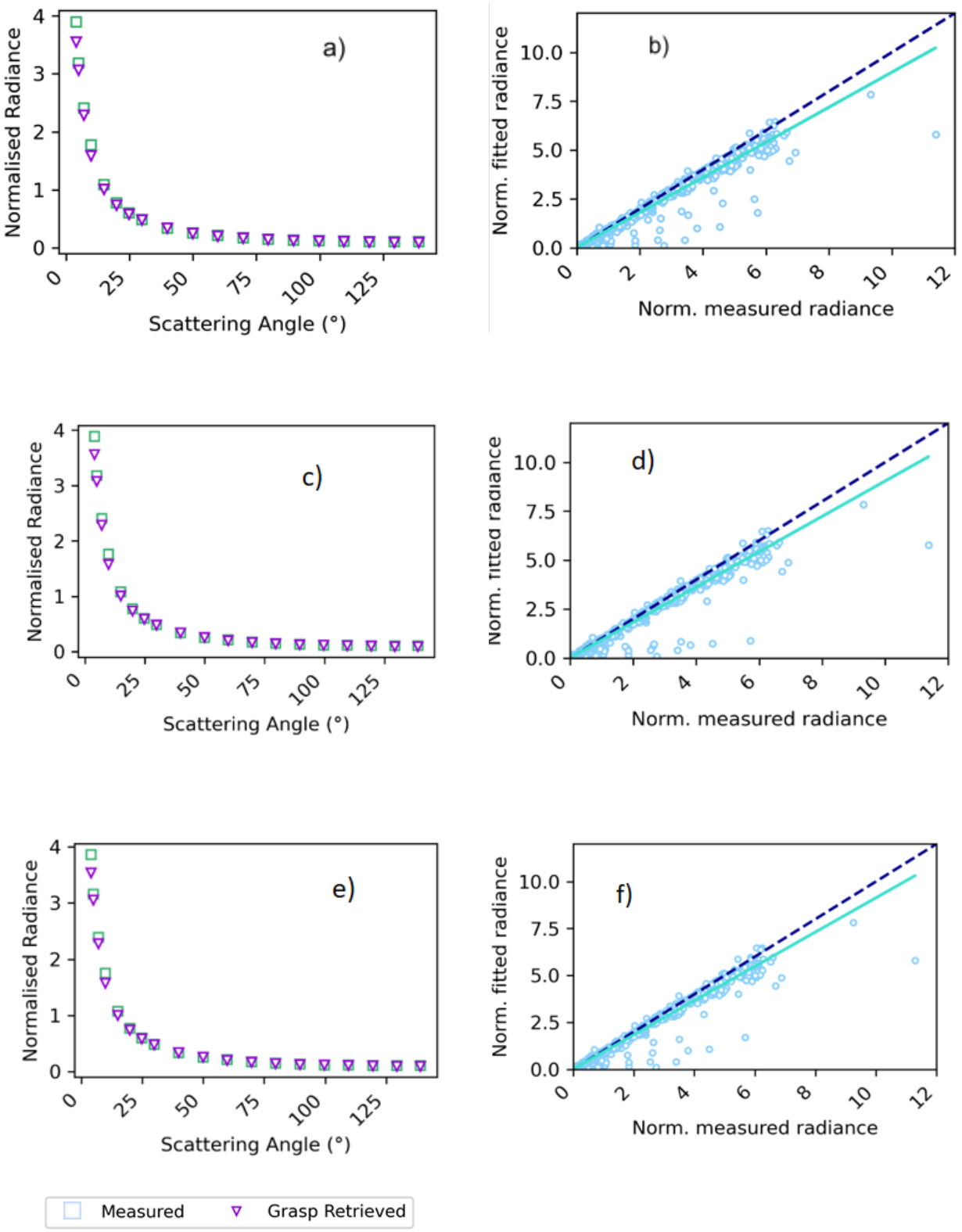


Figure 3.4. Values of the measured (blue squares) and fit (inverted purple triangles) normalised radiance as a function of the scattering angle at 870 nm obtained by processing GRASP using the

set of calibration coefficients provided by ISDC a) and calculated using ILP with MRI c) or the UILP e). The scattering plots for these normalised fitted and measured radiance have also been included. The dashed dark blue line indicate the perfect agreement ($R_{meas} = R_{fit}$), while the linear regression of the data is represented by the cyan line. When the ISDC calibration is used (b), the linear regression is $R_{fit} = 0.869\, R_{meas} + 0.020$, with $R^2 = 0.963$; for the ILP with MRI (d), it is $R_{fit} = 0.903\, R_{meas} + 0.014$, with $R^2 = 0.962$; and for the UILP (f), it is $R_{fit} = 0.912\, R_{meas} + 0.016$, with $R^2 = 0.968$.

3.4.2. Comparison of SSA

Before proceeding to the comparison of the Volume Size Distribution retrieved by the different algorithms applied to Prede and Cimel measurements, it is interesting to study the discrepancies in the Single Scattering Albedo (SSA). Figure 3.5 depicts the time evolution of the SSA at 443 a) and 1020 b) nm on August 16 obtained using different inversion algorithms. The Skyrad 4.2, 5 and MRI inversions are derived from Prede data, while the AERONET retrievals are obtained from Cimel measurements. The GRASP algorithm is applied either to Cimel and Prede data. Furthermore, Table 3.2 contains the main statistics (RMSE, standard deviation, MBD and R^2) for the SSA differences at 443 nm with respect to GRASP Prede inversion. Ideally, these differences should be computed using simultaneous measurements. However, the limit in the time difference for SSA retrievals from Prede data has been set to 60 s in order to keep enough data to compute the statistics. In the case of the Cimel-based retrievals, the few timestamps available force to relax the criterion for the time difference, that has been set to 300 s (AERONET) and 360 s (GRASP Cimel). Even with this, the number of available retrievals were only 2 and 3 for AERONET and GRASP Cimel inversions, respectively. The statistics for these cases are thus very poor, so the interpretation of the results have to be handled with care.

As it can be noticed when comparing Figures 3.5a and 3.5b, the discrepancies between algorithms in the retrievals of SSA at 443 nm are higher than at the other channels. This is related to the larger errors in the inversion that are associated with this wavelength. Despite this, the corresponding statistics for the differences indicate a reasonably good agreement between inversion procedures. Dubovik et al. 2000 estimated an uncertainty of 0.03 for the SSA_{400} in a dusty environment. The RMSE values in Table 3.2 range between 0.01 and 0.04, i.e. of the order of this uncertainty, although the differences for Skyrad MRI v2 and Skyrad 4.2 slightly exceed it. It has to be taken into account, however, that SSA retrievals from GRASP applied to Prede data are the ones that differ the most from the other results, being these differences much less significant at the 1020 nm channel (see Figure 3.5).

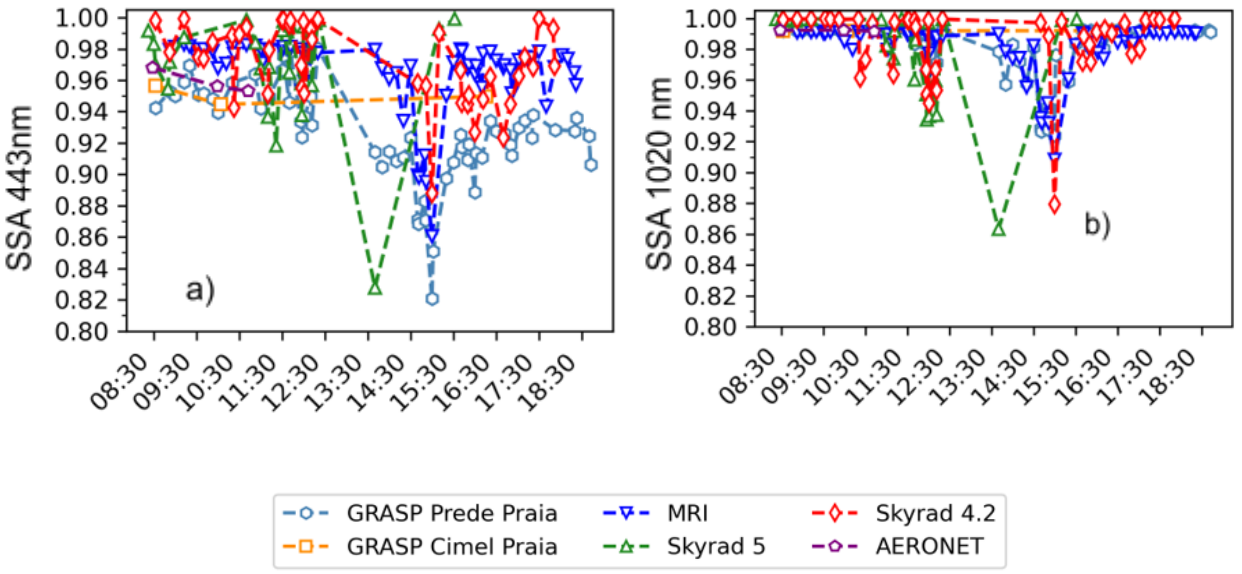


Figure 3.5. *Evolution over time of the SSA_{443} a) and SSA_{1020} b) obtained by the different inversion algorithms using measurements from August 16.*

Table 3.2 Values of the statistics (RMSE, std, MBD and R^2) for the differences in SSA_{443} between each inversion algorithm and the values retrieved from GRASP inversion based on Prede data. The time difference criterion between the retrieved SSA have been indicated, along with the number of timestamps that passed these criteria and thus were included in the computation of the statistics. Notice that the R^2 of AERONET is meaningless, since only two points are available.

	AERONET	GRASP Cimel	Skyrad MRI v2	Skyrad 5	Skyrad 4.2
RMSE	0.022	0.012	0.040	0.031	0.041
DIFF STD	0.004	0.005	0.016	0.016	0.017
MBD	0.021	0.012	0.037	0.017	0.037
R^2	1.000	0.214	0.703	0.623	0.751
Δt **(s)**	300	360	60	60	60
N	2	3	54	17	32

3.4.3. Comparison of Volume Size Distribution

Figure 3.6 shows the curves representing the Volume Size Distribution obtained using the different inversion algorithms, along with the distribution integrated from in-situ measurements. Specifically, for inversions based on Prede or Cimel data, the dV/dlnr values for each radius correspond to the average dV/dlnr obtained during the flight time, that is, when in-situ measurements are available. All the distributions, including in-situ, are similar in the range $0.15\,\mu m < r < 6\,\mu m$. The distributions processed by GRASP using data from Prede and Cimel deserve special attention, as they are very similar, despite the measurements belonging to different instruments. The higher discrepancies with respect to in-situ appear at the edges of the distributions due to the constraints introduced in the inversion procedure for stabilising the solutions. Indeed, it can be noticed that, unlike its successors, the Skyrad 4.2 procedure does not impose any maximum limits to their solutions.

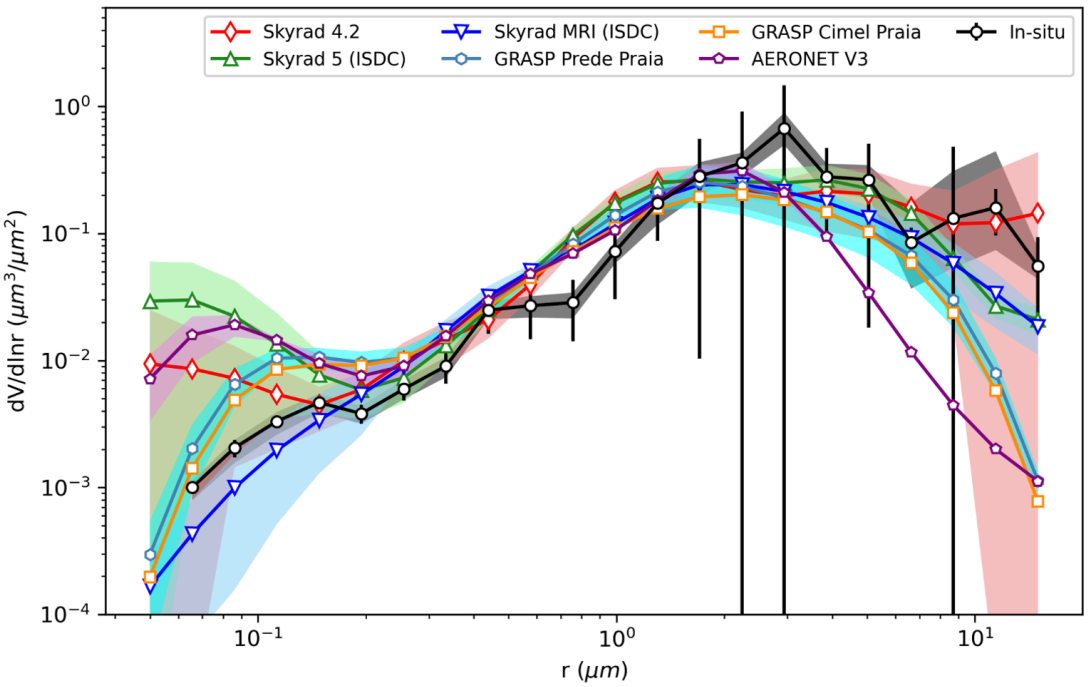


Figure 3.6. Volume Size distributions obtained from the inversion of Prede (Skyrad 4.2, 5, MRI and GRASP) and Cimel (AERONET and GRASP) almucantar measurements, along with the integrated in-situ measurements. The dV/dlnr points have been computed as an average of the retrievals during the time of flight (from 14:45 to 19:01h on August 16), while the shadows represent the standard deviation of the retrievals.

Following the approach used for SSA in Section 2.2.3.2, based on the comparison of simultaneous (or at least the closest in time) SSA retrievals from the different algorithms with respect to GRASP Prede inversions, the Volume Size Distributions have been also compared in a similar way. In particular, Figure 3.7a displays jointly all the distributions obtained based on Prede measurements. The timestamps that pass the Skyrad 5 algorithm differ considerably in time with the timestamps from the other algorithms. Therefore, the maximum time difference between the distributions had to be set to 500 s. The Volume Size Distributions obtained from MRI and GRASP procedures are the ones which agree the most. In addition, what has been mentioned about the solutions from the Skyrad 4.2 procedure not being constrained can be seen at $r > 10\ \mu m$.

Furthermore, Table 3.3 complements Figure 3.7a by displaying the statistics for the dV/dlnr differences with respect to the GRASP Prede measurements. As it can be visually spotted in Figure 3.7a, the best agreement in dV/dlnr of Prede GRASP is with MRI, and the discrepancies with respect to Skyrad 4.2 are the largest. However, the RMSE is in every case much smaller than 0.1, which is the error estimated based on Dubovik et al. 2000 for Volume Size Distributions measured in dusty environments.

Table 3.3 Values of the statistics (RMSE, std, MBD and R^2) computed for the differences in the Volume Size Distributions obtained between the Skyrad 4.2, 5 and MRI algorithms with respect to GRASP Prede inversions.

	Skyrad MRI v2	Skyrad 5	Skyrad 4.2
RMSE ($\mu m^3/\mu m^2$)	0.015	0.050	0.073
DIFF STD ($\mu m^3/\mu m^2$)	0.010	0.042	0.057
MBD ($\mu m^3/\mu m^2$)	0.007	0.022	0.034
R^2	0.963	0.892	0.416

Finally, Figure 3.7b shows the comparison of Volume Size Distributions obtained from Cimel measurements (AERONET and GRASP Cimel) with the GRASP Prede inversions. The Skyrad MRI v2 inversion has also been added. In this case, the maximum time difference between the datasets is 270 s, corresponding to the difference between Cimel and Prede measurements. As it had been previously seen in Figure 3.6, the best agreement between size distributions is obtained for Cimel and Prede data processed with the GRASP

algorithm. Furthermore, it is important to remark that the discrepancies between all the algorithms are very small at $r < 1\,\mu m$. Analogously to Table 3.3, Table 3.4 contains the main statistics computed based on the dV/dlnr differences with respect to the GRASP Prede measurements. Notice that the values with respect to the Skyrad MRI v2 are different from Table 3.3, as here the time difference between distributions is smaller, so a different timestamp is being compared. In any case, the RMSE is also much smaller than 0.1, so it can be stated that there is a very good agreement between the dV/dlnr obtained by the different algorithms and instruments.

Table 3.4 Values of the statistics (RMSE, std, MBD and R^2) computed for the differences in the Volume Size Distributions obtained between the Skyrad MRI, AERONET and GRASP Cimel with respect to GRASP Prede inversions.

	Skyrad MRI v2	AERONET	GRASP Cimel
RMSE ($\mu m^3/\mu m^2$)	0.047	0.021	0.015
DIFF STD ($\mu m^3/\mu m^2$)	0.036	0.015	0.012
MBD ($\mu m^3/\mu m^2$)	0.022	0.001	0.006
R^2	0.786	0.937	0.969

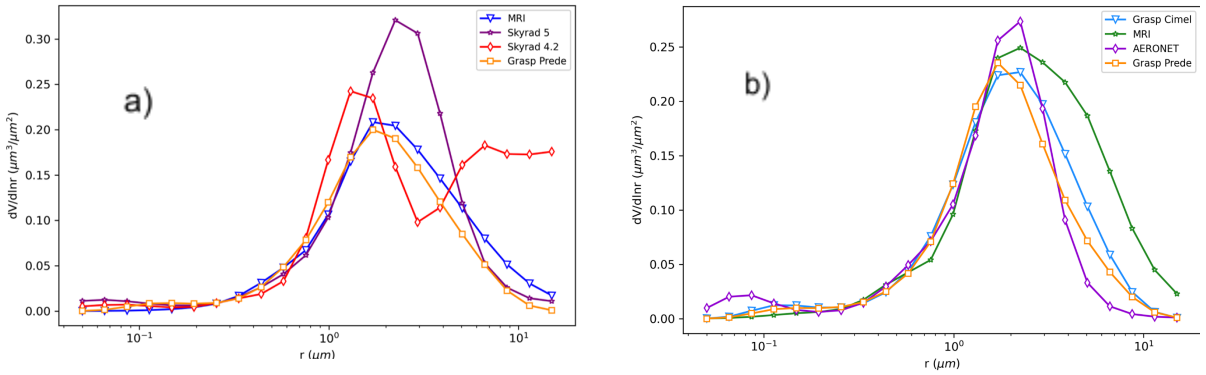


Figure 3.7. *a) Volume Size Distributions obtained from the inversion algorithms based on Prede measurements, with a maximum difference in the timestamps of 500 s (minimum difference timestamp found between Skyrad 5 and the other algorithms). b) Volume Size Distributions from the inversions based on Cimel data, with MRI and GRASP Prede dV/dlnr added for comparison. In this case, the maximum difference of the timestamps is 270 s.*

3.5 Conclusions

In this study, data from the SAVEX-D campaign has been used in order to compare aerosol optical properties using different inversion algorithms and instruments in a dusty environment (the Cape Verde archipelago). The advantage of measuring under such conditions lies in the fact that higher AOD values ensure good conditions for the inversion.

As first step, taking into account that the raw dataset of Prede measurements allowed the computation of the calibration coefficients based on different methodologies (ILP using MRI and UILP), apart from the set of coefficients provided by the ISDC, it has been possible to perform a small test to find out which set yielded better results in the inversion. Then, based on the differences between the measured and fit radiances, it has been concluded that among the different calibration methods, the UILP routine leads to slightly smaller residuals in the inversion.

Next, the SSA obtained as a result from the different inversions has been studied, finding a generally good agreement between the algorithms. However, as expected, higher discrepancies have been obtained at 443 nm, due to the higher uncertainties in the inversion.

Finally, the Volume Size Distributions obtained by the different algorithms have been compared to in-situ measurements. Then, it has been found that for the interval of radii $0.15\ \mu m < r < 6\ \mu m$, all the algorithms yield very similar size distributions.

Moreover, it has been verified that the best agreement between Volume Size Distributions is obtained when comparing Cimel and Prede data processed using GRASP algorithm. This is a very promising result towards the harmonisation of measurements from different instruments, as these distributions have been obtained using the same algorithm applied to data collected by instruments from different networks: AERONET (in the case of the Cimel) and SKYNET (in the case of the Prede).

References:

- Dubovik, Oleg & Smirnov, Alexander & Holben, Brent & King, Michael & Kaufman, Y.J. & Eck, Thomas & Slutsker, I.. (2000). Accuracy assessment of aerosol optical properties retrieved from Aerosol Robotic Network (AERONET) Sun and sky radiance measurements. Journal of Geophysical Research. 105. 9791-9806. 10.1029/2000JD900040.
- Dubovik, Oleg & Lapyonok, Tatyana & Litvinov, Pavel & Herman, Maurice & Fuertes, David & Ducos, Fabrice & Torres, Benjamin & Derimian, Yevgeny & Huang, Xin & Lopatin, Anton & Chaikovsky, Anatoli & Aspetsberger, Michael & Federspiel, Christian. (2014). GRASP: a versatile algorithm for characterizing the atmosphere. SPIE Newsroom. 10.1117/2.1201408.005558.
- Giles, D. M., Sinyuk, A., Sorokin, M. G., Schafer, J. S., Smirnov, A., Slutsker, I., Eck, T. F., Holben, B. N., Lewis, J. R., Campbell, J. R., Welton, E. J., Korkin, S. V., and Lyapustin, A. I.: Advancements in the Aerosol Robotic Network (AERONET) Version 3 database – automated near-real-time quality control algorithm with improved cloud screening for Sun photometer

aerosol optical depth (AOD) measurements, Atmos. Meas. Tech., 12, 169–209, https://doi.org/10.5194/amt-12-169-2019, 2019.

- Hashimoto, M., Nakajima, T., Dubovik, O., Campanelli, M., Che, H., Khatri, P., Takamura, T., and Pandithurai, G.: Development of a new data-processing method for SKYNET sky radiometer observations, Atmos. Meas. Tech., 5, 2723–2737, https://doi.org/10.5194/amt-5-2723-2012, 2012.
- Kumar, G., Momoi, M., Campanelli, M., Garcia-Suñer, M., Kouremeti, N., Kudo, R., Pedrós, R., and Estellés, V.: Optimization of the SKYNET calibration with an iterative Improved Langley method and its validation in the Mediterranean area, EGUsphere [preprint], https://doi.org/10.5194/egusphere-2026-4267, 2026.
- Kudo, R., Diémoz, H., Estellés, V., Campanelli, M., Momoi, M., Marenco, F., Ryder, C. L., Ijima, O., Uchiyama, A., Nakashima, K., Yamazaki, A., Nagasawa, R., Ohkawara, N., and Ishida, H.: Optimal use of the Prede POM sky radiometer for aerosol, water vapor, and ozone retrievals, Atmos. Meas. Tech., 14, 3395–3426, https://doi.org/10.5194/amt-14-3395-2021, 2021.
- Nakajima, T., Tonna, G. and Rao, R. et al., 1996. Use of sky brightness measurements from ground for remote sensing of particlulate polydispersions, Appl. Opt., 35, pp. 2672-2686.
- Sinyuk, A., Holben, B. N., Eck, T. F., Giles, D. M., Slutsker, I., Korkin, S., Schafer, J. S., Smirnov, A., Sorokin, M., and Lyapustin, A.: The AERONET Version 3 aerosol retrieval algorithm, associated uncertainties and comparisons to Version 2, Atmos. Meas. Tech., 13, 3375–3411, https://doi.org/10.5194/amt-13-3375-2020, 2020.

4. Initial evaluation of photometer radiance and normalized radiance measurements in the NIR region (1627 nm and 2200 nm for PREDE-POM).

4.1 The database

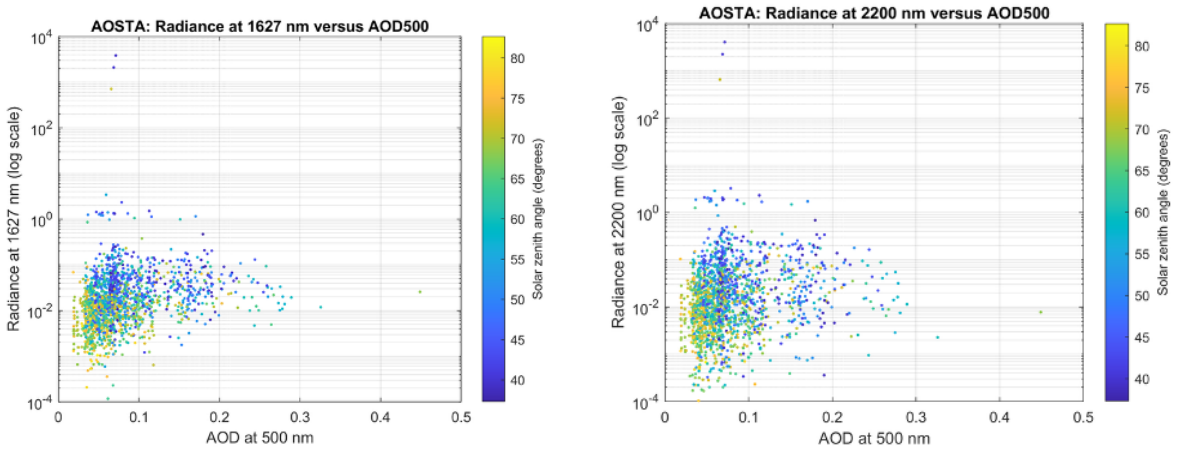
A very preliminary evaluation of the shortwave-infrared sky-radiance measurements at 1627 nm and 2200 nm channels from the SKYNET sun–sky radiometers model POM02 was performed in Aosta, a semi-urban Alpine station situated at 570 meters above sea level in Italy, and Takayama, at 1437 meters above sea level in Japan. The period extends from 1 January 2025 4 to 30 April 2025 for Aosta and from 1 January to 31 December 2025 for Takayama.

The sky diffuse radiance observations and the AOD at 500 nm (AOD500) from direct irradiance within 10 minutes were selected and a representative radiance measured at 30° of scattering angles (SCA) was used in the time-series analysis.

4.2 Results

4.2.1 Radiance dependences

The dependance of the radiance at SCA = 30° on AOD500 at several solar zenith angles was analysed for both sites (Figure 4.1), showing the two variables are almost not correlated.



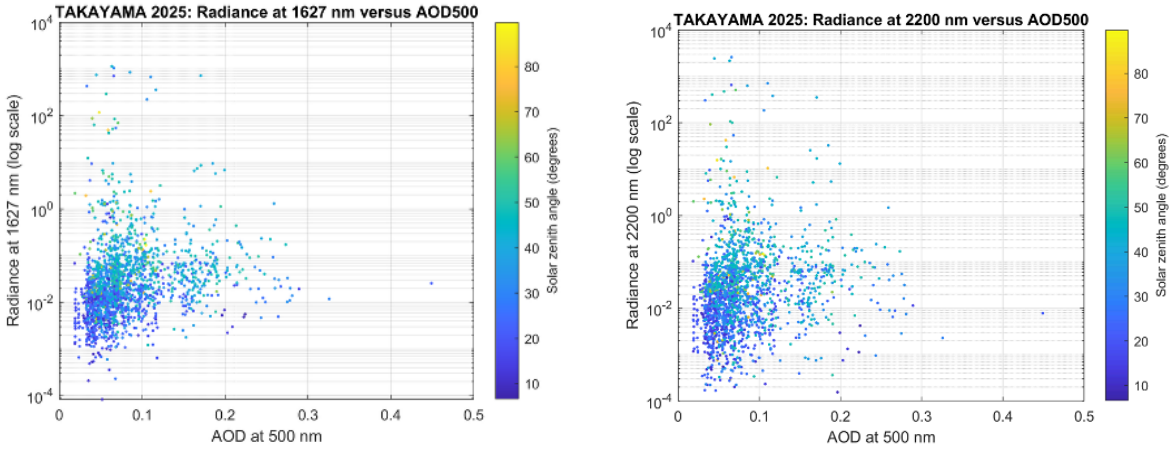


Figure 4.1 The dependance of the radiance at SCA = 30° on AOD500 at several solar zenith angles was analysed for Aosta (top) and Takayama (bottom) at the two wavelengths

The dependence on the Solar zenith angles was also analysed (Fig 4.2) for different AOD500 values. A slight decreasing trend with respect to the solar zenith angles was observed in Aosta and increasing in Takayama. The difference between the two sites could be related to the presence of snow in the later, but it should be analysed inside.

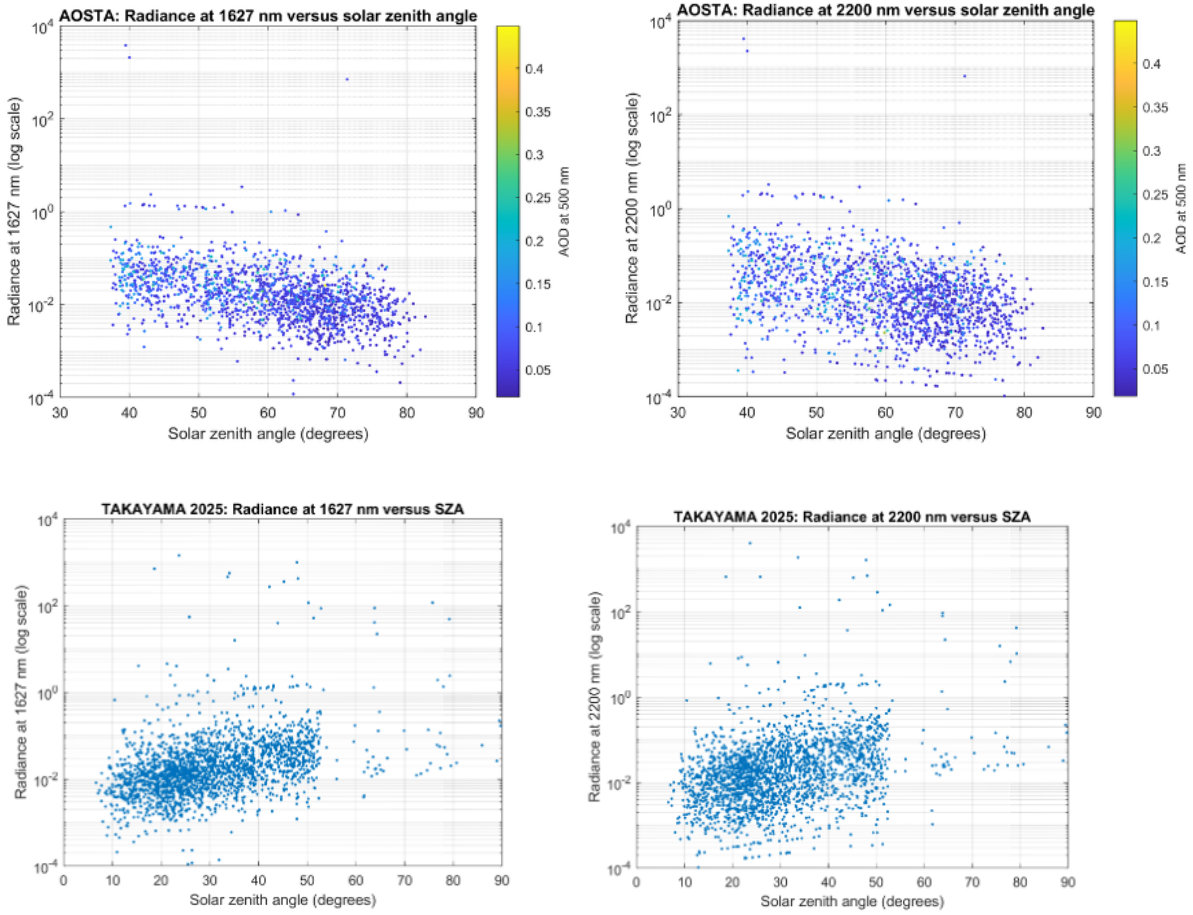
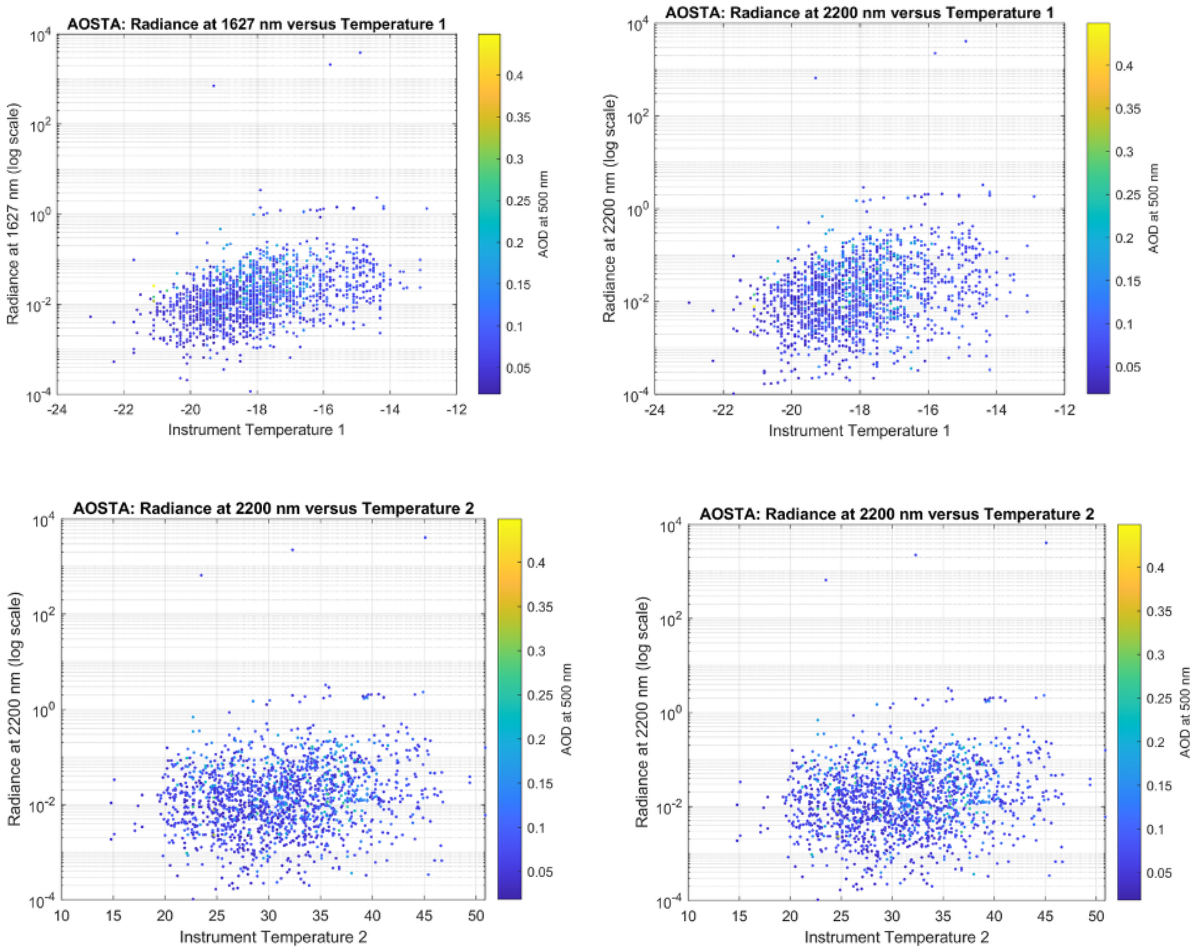


Figure 4.2 The dependance of the radiance at SCA = 30° on the Solar zenith angles

Finally the temperature dependence was investigated both for the SWIR region (T1) where it is cooled and for the VIS region (T2) when the optics are heated (Figure 4.3). A slight increasing dependence on increasing temperature is observed for both the wavelengths (but mostly for the 1627 nm) in the case of the cooling system, in both sites. No evidence of a slope exists in the case of the heating system.



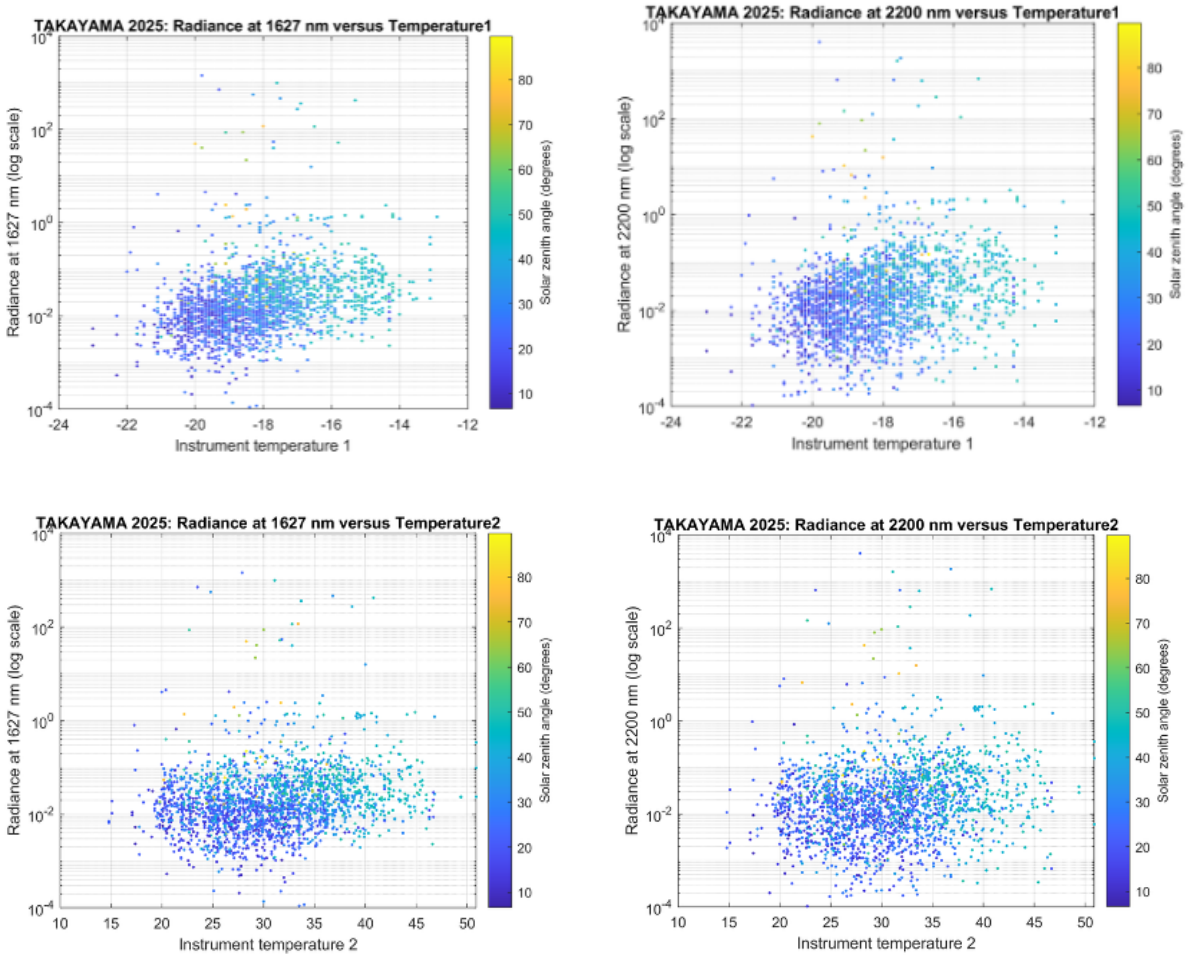


Figure 4.3 Radiance dependence on the internal cooled and heated temperatures.

5. Calibration of Near-Infrared Channels of PREDE-POM Sun Photometers Using Standard and on Site Langley Plot Methods

5.1 Introduction

We calibrated the two near infrared (NIR) wavelengths (1627 and 2200 nm), of a PREDE-POM02 sun photometer located in Takayama Observatory, Japan (36.056° N, 140.125° E; altitude 1.4 km) using the standard Langley plot techniques on three selected clear-sky days in early 2025. For these two channels water vapor absorption has been taken into account (Uchiyama et al., 2018). The standard Langley was also applied to the visible and shortwave-infrared channels (340–1020 nm) producing excellent linear fits ($R^2 > 0.93$), while the NIR channels showed larger scatter ($R^2 = 0.50–0.81$) probably due to lower signal-to-noise and stronger atmospheric variability. The retrieved V_0 values are internally consistent across the selected calibration days, showing day-to-day variations of approximately 8% at 1627 nm and 6% at 2200 nm.. Our results confirm that on-site NIR calibration is feasible, though improved water vapour data and more sampling days are needed to reduce uncertainty. The work contributes directly to the objectives of the SKYNET network and its European sub-network, ESR, by extending harmonised aerosol products beyond 1020 nm.

SKYNET has long provided harmonized aerosol optical depth (AOD) up to 1020 nm. The near-infrared (NIR) channels at 1627 and 2200 nm, however, have remained underexploited because their calibration is more difficult. Extending harmonized aerosol products to longer wavelengths is a key objective of HARMONIA Working Group 2, and it also aligns with SKYNET's broader goal of improving aerosol characterization for climate studies.

5.2. Instrument and data

We used direct-beam irradiance measurements from a PREDE-POM sun photometer on three clear-sky days: 18 January, 15 February, and 25 February 2025. The wavelengths analyzed were 340, 400, 500, 675, 870, 1020, 1627, and 2200 nm Takayama Observatory, Japan (36.056° N, 140.125° E; altitude 1.4 km)

5.3. File validation before calibration

Before running any Langley fit, we followed a fixed sequence of checks. First, we inspected the raw sun photometer file, containing sun direct irradiance measurements, for completeness, timestamp consistency, and correct header information. This ensures that the measurement series is intact and that no data are missing or corrupted. Second, we checked the **dt4** file, containing sky

radiances retrieved by the Skyrad_MRI model (Kudo et al., 2021) from the almucantar measurements to confirm the specific measurement used, verify the solar geometry, and ensure the sky-radiance values are correctly formatted. Because the retrieved radiances are also cloud screened, the cross check of direct measurements and dt4 output, allowed to select days with clear sky . Only after both checks passed did we run the Langley equation on the screened data. This order matters because the dt4 file provides the direct-beam and sky-radiance inputs that feed the smoothness check and the retrieval; if the sun file or dat file is inconsistent, the dt4 file may inherit that inconsistency, and any subsequent Langley fit will be biased.

5.4. Langley plot technique

For non-absorbing channels, the standard Langley method follows the Beer–Lambert–Bouguer law:

$$\ln(V) = \ln(V_0) - m_0\tau_{\text{total}}$$

where V is the measured signal, V0 the extraterrestrial constant, m0 the air mass, and t_total the total optical depth. For the NIR channels, water vapor absorption is significant. We therefore constructed a modified Langley plot, following the approach of Uchiyama et al. (2018):

$$Y = \ln(V) + m_0\tau_{\text{PWV}} = \ln(V_0) - m_0\left(\tau_{\text{aer}} + \tau_{\text{Rayleigh}}\right)$$

Here $\tau_{\text{PWV}}$is the water vapor optical depth, computed from PWV using fixed coefficients: 4.2×10^{-5}at 1627 nm and 1.9×10^{-5}at 2200 nm.

The water vapor optical depth $\tau_{_PWV}$ was computed using the SKYRAD_MRI simulation code (Kudo et al., 2021), which was run with a climatological precipitable water vapor (PWV) content representative of the Takayama site for the measurement season. The code provided the spectral water vapor optical depth at 1627 and 2200 nm, which was then used to construct the modified Langley variable Y using a climatological wv content. The intercept of versus gives , and the slope gives the negative of the aerosol-plus-Rayleigh optical depth**.**

5.3. Screening and outlier removal

We restricted the air mass range to $2.0 \leq m_0 \leq 5.0$. An initial Langley regression was performed using all measurements within this range. If the root mean square deviation (RMSD) exceeded 0.006, the point with the largest residual was removed and the regression was repeated. This iterative screening procedure continued until the RMSD threshold was satisfied. The number of fitting cycles required to obtain the final solution is reported in Table 1 under the column **"iter"**. In addition, we performed a direct-beam smoothness check to identify periods of unstable atmospheric conditions using the 675 nm wavelength because it is largely free from strong gaseous absorption and is less affected by Rayleigh scattering than the shorter wavelengths, making it a reliable indicator of atmospheric stability during Langley calibration.

5.4. Results

5.4.1 Fit quality

The visible and shortwave-infrared channels behaved as expected. At 340, 400, and 500 nm, the fits were excellent (R^2 > 0.998, RMSD < 0.013). The 675, 870, and 1020 nm channels also produced good linearity (R^2 = 0.93–0.99).

The NIR channels were more challenging. At 1627 nm, R^2 ranged from 0.50 to 0.71; at 2200 nm, from 0.60 to 0.81. The larger scatter could be related to the lower signal-to-noise ratio at these wavelengths and to the consideration of a climatological PW value rather than an actual measurement.

5.4.2 Langley Plots: Summary and Discussion

a) Visible and shortwave-infrared channels (340–1020 nm)

Figures 1–6, present the Langley plots for 340, 400, 500, 675, 870, and 1020 nm. The quantitative fit statistics in Table 1 match the visual impression from these figures.

At **340 nm (Figure 1)**, the individual-day fits are excellent (), but the combined plot shows clear separation between the three dates. The table confirms this: varies from (18 Jan) to (25 Feb), a spread of more than 50%. The slope also changes from 0.612 to 0.563. This is consistent with the strong sensitivity of the 340 nm channel to Rayleigh scattering, which depends on pressure and temperature, and to day-to-day atmospheric variability. Outlier removal was aggressive: 12 points reduced to 3 on 18 Jan, 11 to 5 on 15 Feb, and 9 to 4 on 25 Feb. This improves the fit but reduces the robustness of the intercept.

At **400 nm (Figure 2)** and **500 nm (Figure 3)**, the fits remain excellent (at 400 nm, at 500 nm), and the three dates converge more closely in the combined plots. The values are more stable: at 500 nm they range from to , a spread of about 13%. The 25 Feb data required no outlier removal at 400 or 500 nm, suggesting stable conditions on that day.

At **675 nm (Figure 4)**, the fits are good (–0.995) and the combined plot shows the three dates almost overlapping. is tightly constrained: to . No outlier removal was needed on any date (Ninit = Nfin). This indicates a stable instrument response and a well-defined slope.

At **870 nm (Figure 5)**, linearity is moderate (–0.974). The slopes are small (0.0128–0.0173), and ranges from to . The combined plot shows some scatter but no large offsets. No outliers were removed.

At **1020 nm (Figure 6)**, linearity is good but slightly lower than at 675 or 870 nm (–0.944). The slopes are very small (0.0070–0.0105), so the intercept is less well constrained. ranges from to . No outlier removal was needed, but the lower indicates that the signal-to-noise ratio and residual water-vapour absorption are beginning to affect the fit.

b) Near-infrared channels (1627 and 2200 nm)

Figures 7 and 8 show the Langley plots for 1627 and 2200 nm. These are the most challenging channels, and Table 1 quantifies the difficulty.

At **1627 nm (Figure 7)**, it ranges from 0.50 to 0.71. The slopes are extremely shallow (0.0021–0.0040), meaning that changes very little with air mass. As a result, the intercept is poorly constrained. No outliers were removed on any date (Ninit = Nfin), yet the scatter remains large. This shows that the problem is not a few outliers but intrinsic noise: low signal-to-noise, low aerosol optical depth, and variable water-vapour absorption. The derived values are (18 Jan), (15 Feb), and (25 Feb), a day-to-day variation of about 8%.

At **2200 nm (Figure 8)**, the situation is similar. ranges from 0.60 to 0.81. Slopes are again very small (0.0021–0.0050). values are (18 Jan), (15 Feb), and (25 Feb), a variation of about 6%. The combined plot shows both scatter within each date and offsets between dates. As with 1627 nm, no outlier removal was applied, confirming that the scatter is inherent to the measurement and atmospheric conditions.

These findings are consistent with the general difficulty of NIR calibration noted by Uchiyama et al. (2018), who found that the 1627 and 2200 nm channels have gas absorption below 1%. The day-to-day scatter in our NIR values (about 8% at 1627 nm and 6% at 2200 nm) confirms that single-day calibrations are not reliable.

Table 1. Langley fit summary for all wavelengths and dates.

WL_nm	Da	te	Ninit	Nfin	ln(V0)	V0	slope	RMSD	R^2	iter	m0_min	m0_max
340	18	Jan	12	3	-12.414	0.0000041	0.612	0.0094	0.9998	3	2.017	4.471
340	15	Feb	11	5	-12.191	0.0000051	0.586	0.0127	0.9997	2	2.029	4.878
340	25	Feb	9	4	-11.969	0.0000063	0.563	0.0043	0.9999	2	2.110	4.438
400	18	Jan	12	3	-9.433	0.0000801	0.311	0.0037	0.9999	3	2.017	4.471
400	15	Feb	11	5	-9.380	0.0000844	0.302	0.0075	0.9996	2	2.029	4.878
400	25	Feb	9	9	-9.213	0.0000998	0.286	0.0057	0.9993	1	2.110	4.438
500	18	Jan	12	5	-8.360	0.0002339	0.127	0.0049	0.9987	2	2.017	4.471
500	15	Feb	11	5	-8.409	0.0002229	0.127	0.0049	0.9990	2	2.029	4.878
500	25	Feb	9	9	-8.278	0.0002541	0.115	0.0026	0.9991	1	2.110	4.438
675	18	Jan	12	12	-7.951	0.0003522	0.039	0.0043	0.9789	1	2.017	4.471
675	15	Feb	11	11	-8.031	0.0003251	0.041	0.0043	0.9856	1	2.029	4.878
675	25	Feb	9	9	-7.940	0.0003562	0.036	0.0020	0.9946	1	2.110	4.438
870	18	Jan	12	12	-8.253	0.0002604	0.015	0.0027	0.9500	1	2.017	4.471
870	15	Feb	11	11	-8.347	0.0002371	0.017	0.0034	0.9518	1	2.029	4.878
870	25	Feb	9	9	-8.262	0.0002581	0.013	0.0016	0.9741	1	2.110	4.438
1020	18	Jan	12	12	-8.341	0.0002385	0.008	0.0016	0.9359	1	2.017	4.471
1020	15	Feb	11	11	-8.434	0.0002174	0.011	0.0022	0.9443	1	2.029	4.878
1020	25	Feb	9	9	-8.356	0.0002351	0.007	0.0014	0.9349	1	2.110	4.438
1627	18	Jan	12	12	-8.839	0.0001450	0.002	0.0014	0.5627	1	2.017	4.471
1627	15	Feb	11	11	-8.919	0.0001339	0.004	0.0022	0.7130	1	2.029	4.878

1627	*25*	*Feb*	*9*	*9*	*-8.859*	*0.0001422*	*0.003*	*0.0019*	*0.5005*	*1*	*2.110*	*4.438*
2200	*18*	*Jan*	*12*	*12*	*-9.342*	*0.0000877*	*0.004*	*0.0014*	*0.7914*	*1*	*2.017*	*4.471*
2200	*15*	*Feb*	*11*	*11*	*-9.403*	*0.0000825*	*0.005*	*0.0021*	*0.8056*	*1*	*2.029*	*4.878*
2200	*25*	*Feb*	*9*	*9*	*-9.341*	*0.0000878*	*0.002*	*0.0013*	*0.6023*	*1*	*2.110*	*4.438*

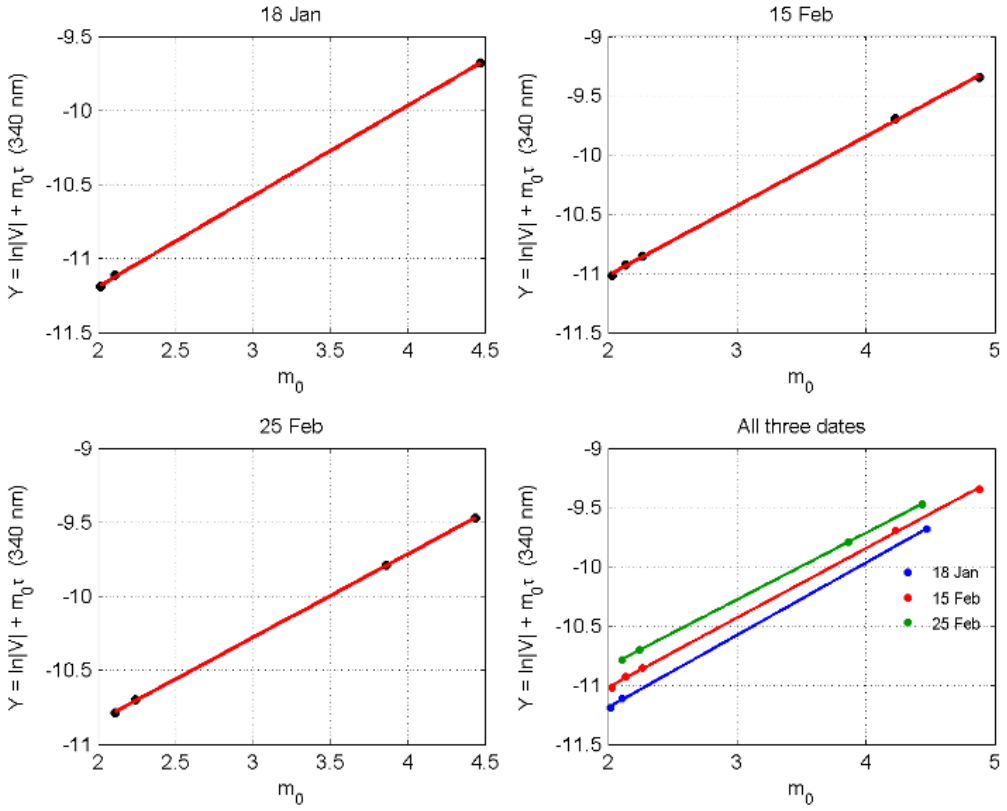


Figure 1: Langley plots at 340 nm (18 Jan, 15 Feb, 25 Feb, and combined)

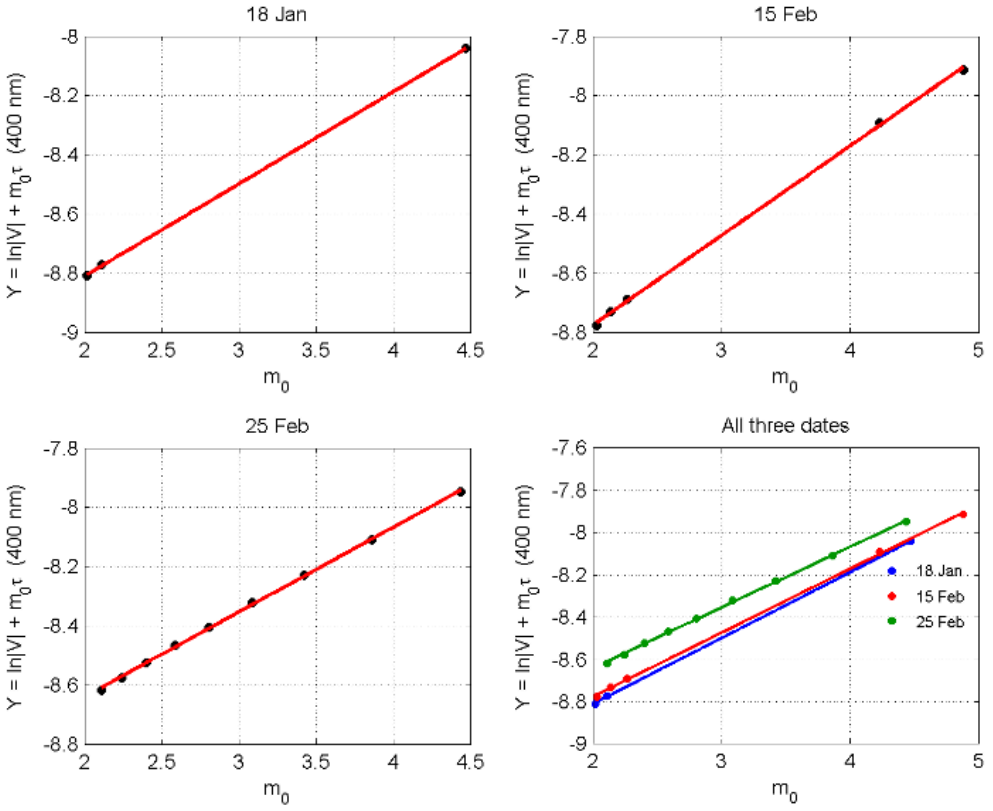


Figure 2: Langley plots at 400 nm (18 Jan, 15 Feb, 25 Feb, and combined)

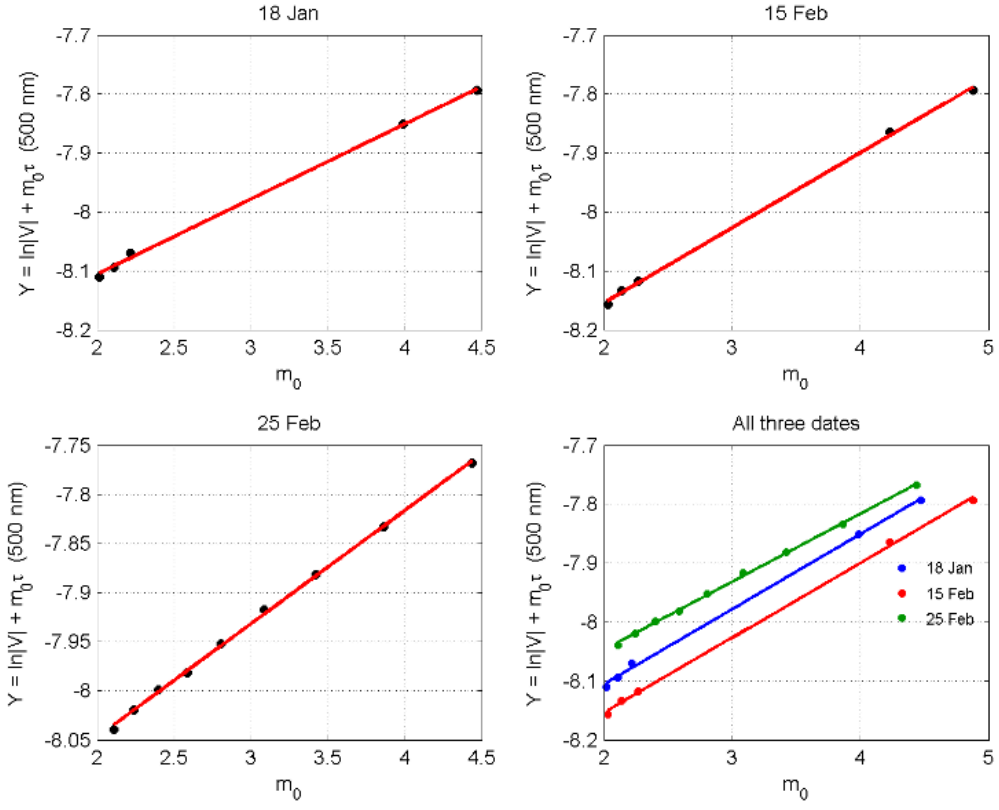


Figure 3: Langley plots at 500 nm (18 Jan, 15 Feb, 25 Feb, and combined)

cost EUROPEAN COOPERATION IN SCIENCE & TECHNOLOGY
Funded by the European Union

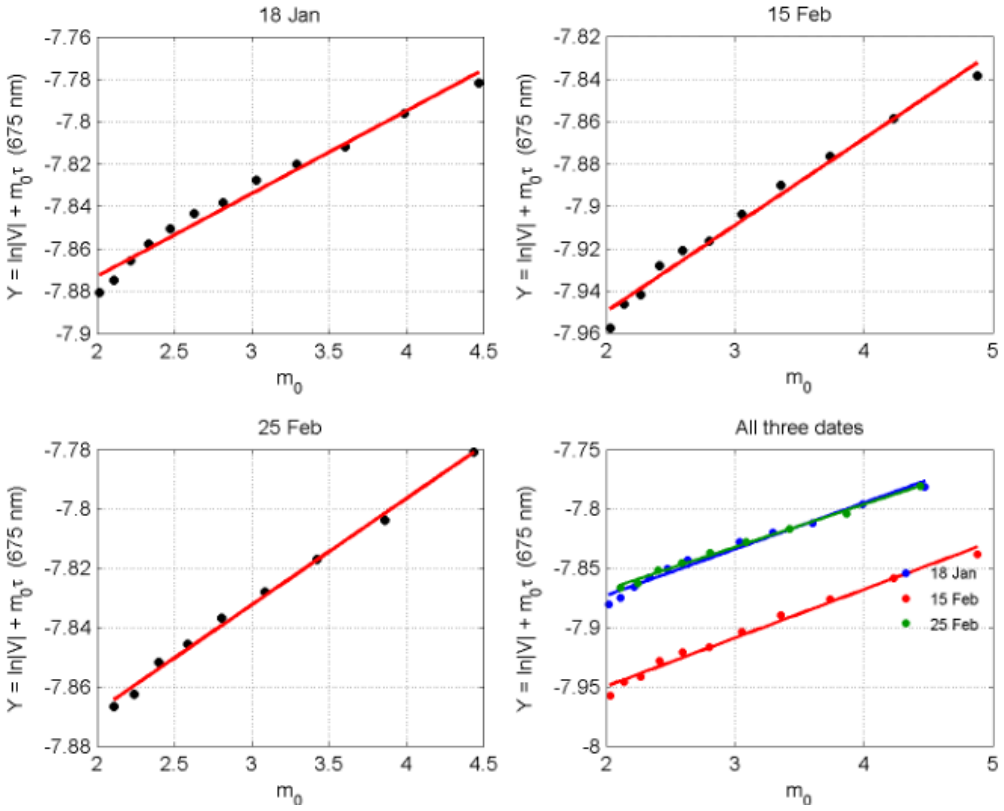


Figure 4: Langley plots at 675 nm (18 Jan, 15 Feb, 25 Feb, and combined)

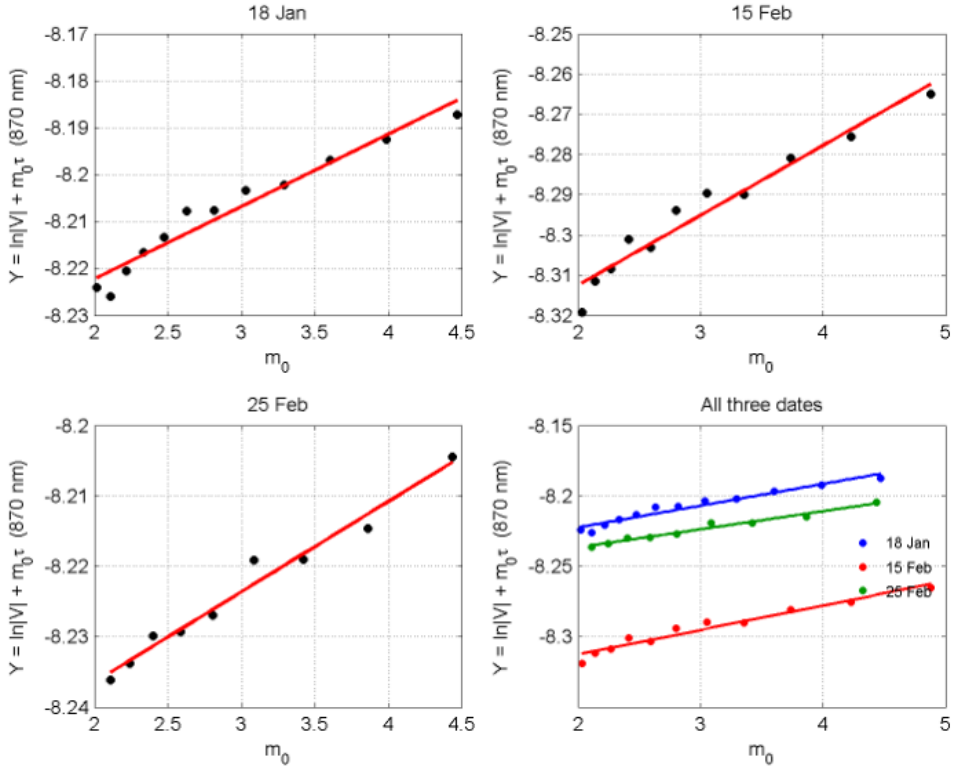


Figure 5: Langley plots at 870 nm (18 Jan, 15 Feb, 25 Feb, and combined)

cost EUROPEAN COOPERATION IN SCIENCE & TECHNOLOGY
Funded by the European Union

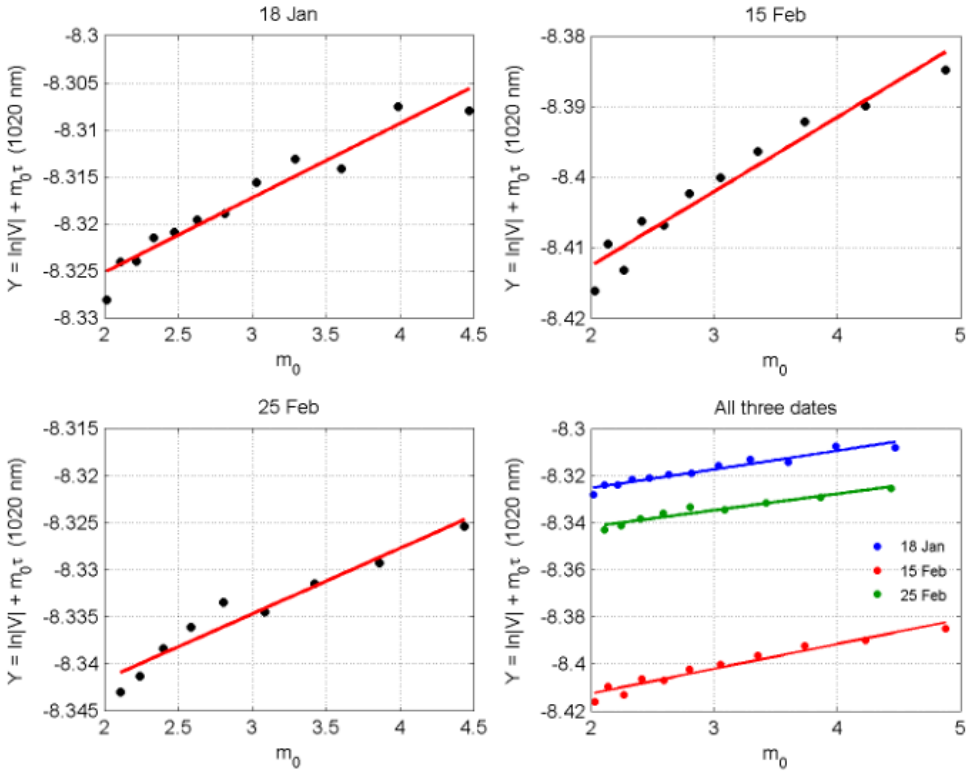


Figure 6: Langley plots at 1020 nm (18 Jan, 15 Feb, 25 Feb, and combined)

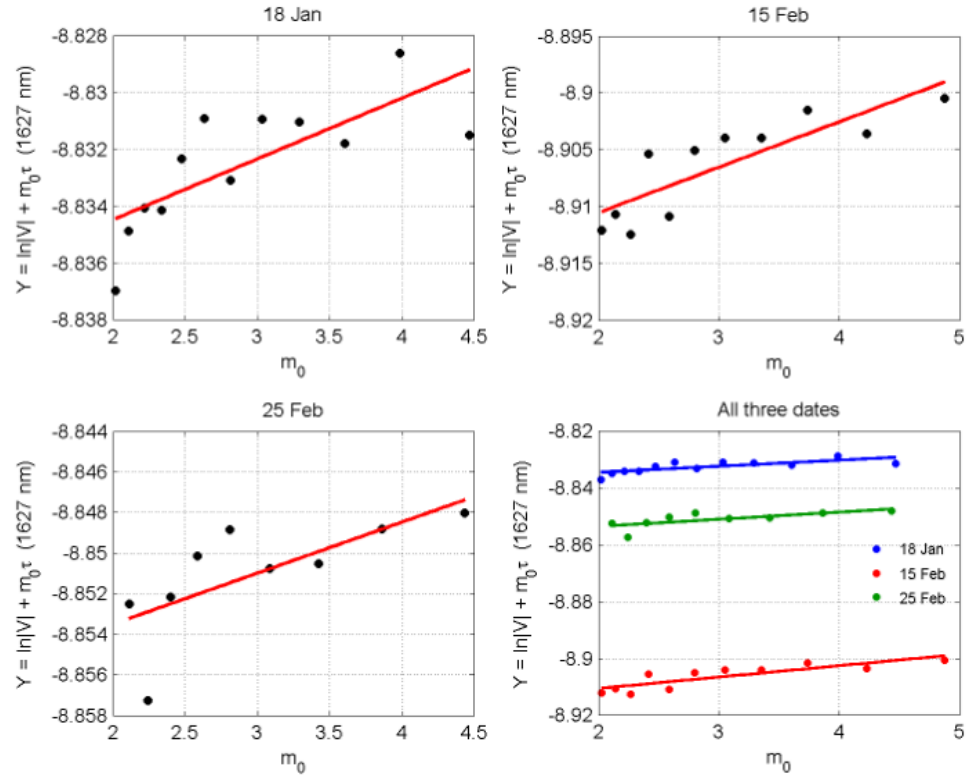


Figure 7: Langley plots at 1627 nm (18 Jan, 15 Feb, 25 Feb, and combined)

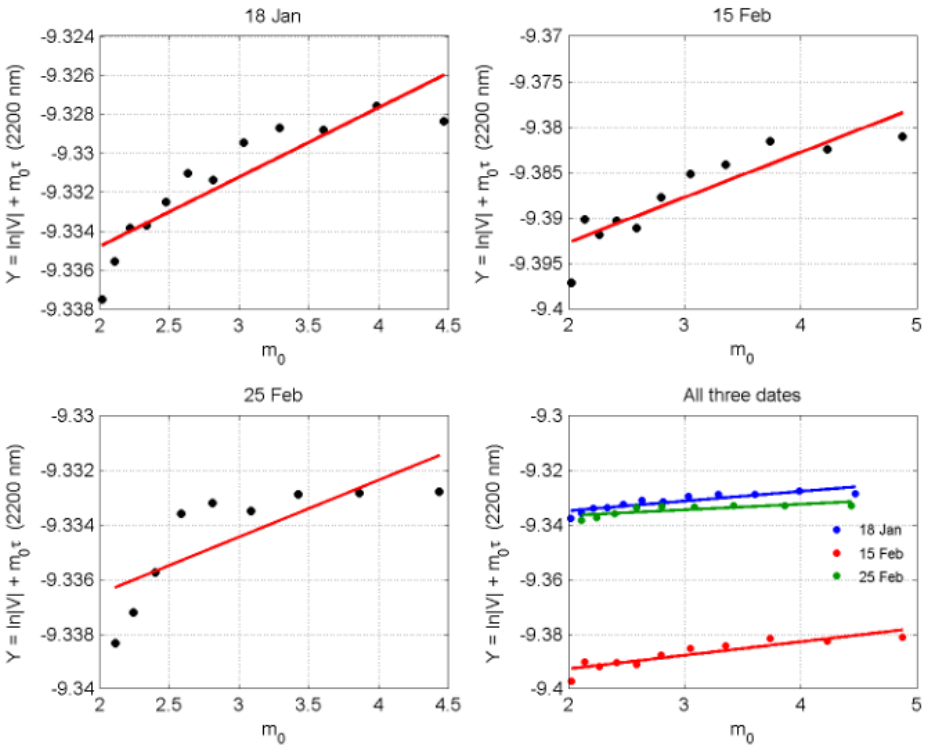


Figure 8: Langley plots at 2200 nm (18 Jan, 15 Feb, 25 Feb, and combined)

These findings obtained with a standard Langley method are however consistent with previous work performed using a modified version of Langley method (Uchiyama et al. (2018)), not set up in this work. He reported that the modified Langley method for the 1225, 1627, and 2200 nm channels required careful selection of dry conditions and ancillary PWV data, and that uncertainties remained higher than for visible channels. They found that the modified Langley method gave V_0 values differing by only 0.8%, 0.4%, and 0.1% from the standard Langley method at 1225, 1627, and 2200 nm, respectively, but the scatter was still larger. The day-to-day scatter in our NIR V_0 values (about 8% at 1627 nm and 6% at 2200 nm) confirms that single-day calibrations are not reliable. For operational use within SKYNET and the ESR network, NIR calibration should be based on multiple days, real-time PWV data, and advanced methods such as SKYMAP (Momoi et al., 2020) or the improved Langley method (Nakajima et al., 1996). This would allow harmonized aerosol products to be extended beyond 1020 nm, directly supporting HARMONIA Working Group 2 and the broader SKYNET objective of improving aerosol–cloud–radiation research.

5.4.3 Derived V0 for NIR channels

Table 2 summarizes the NIR results. The day-to-day variation in is noticeable—about 8% at 1627 nm and 6% at 2200 nm—which points to either instrumental drift or residual atmospheric effects.

Table 2. Derived V_0 for the NIR channels.

Date	V_0 at 1627 nm	V_0 at 2200 nm
18 Jan	1.450×10^{-4}	8.767×10^{-5}
15 Feb	1.339×10^{-4}	8.251×10^{-5}
25 Feb	1.422×10^{-4}	8.778×10^{-5}

5.5. Direct-beam smoothness check

Figures 9–11 show the direct-beam irradiance at 675 nm for the three dates. These plots were used to assess data quality and identify periods of stable atmospheric conditions.

Figure 9. Direct-beam smoothness check at 675 nm for 18 January 2025. The irradiance follows a smooth diurnal curve, with a sharp drop after ~7 hours local time. No points were flagged as outliers, indicating stable conditions during the morning.

Figure 10. Direct-beam smoothness check at 675 nm for 15 February 2025. Several points are flagged (red dots) around 7–8 hours local time, corresponding to a sudden drop in irradiance. These points were excluded from the Langley analysis.

Figure 11. Direct-beam smoothness check at 675 nm for 25 February 2025. One point is flagged at the end of the day (~22 hours local time). The rest of the curve is smooth, indicating stable conditions for most of the measurement period.

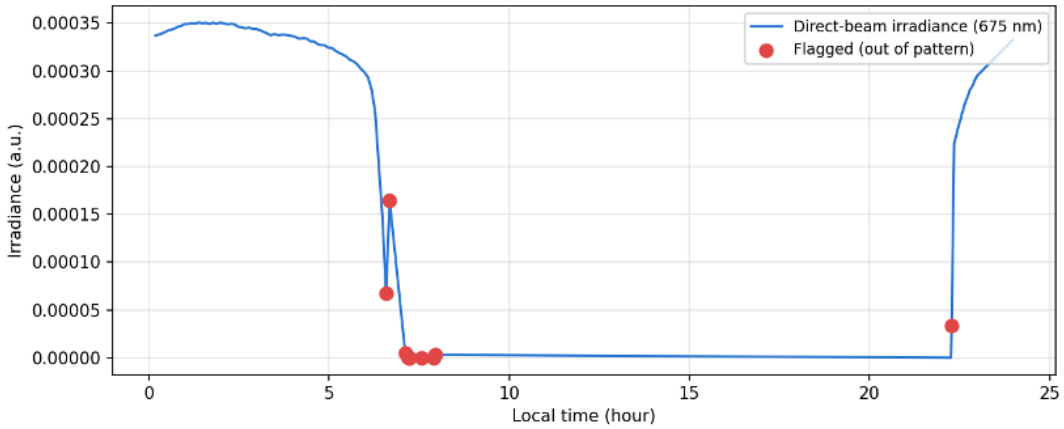


Figure 9: Direct-beam smoothness check at 675 nm for 18 Jan 2025

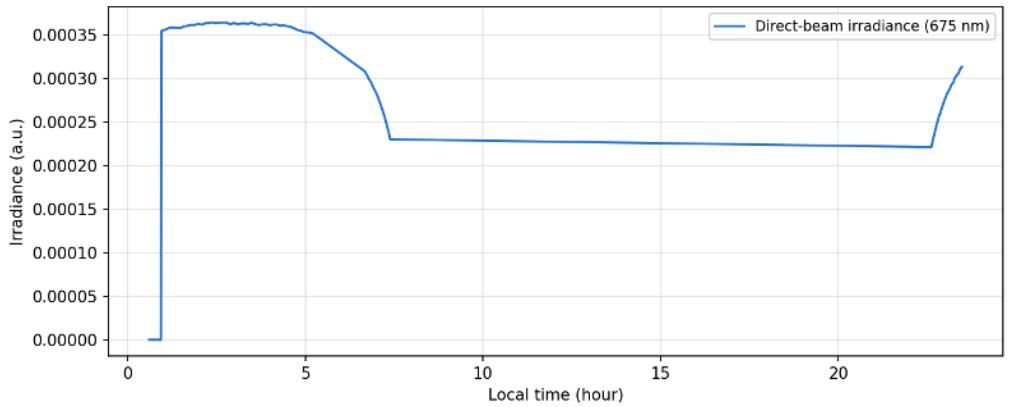


Figure 10 : Direct-beam smoothness check at 675 nm for 15 Feb 2025

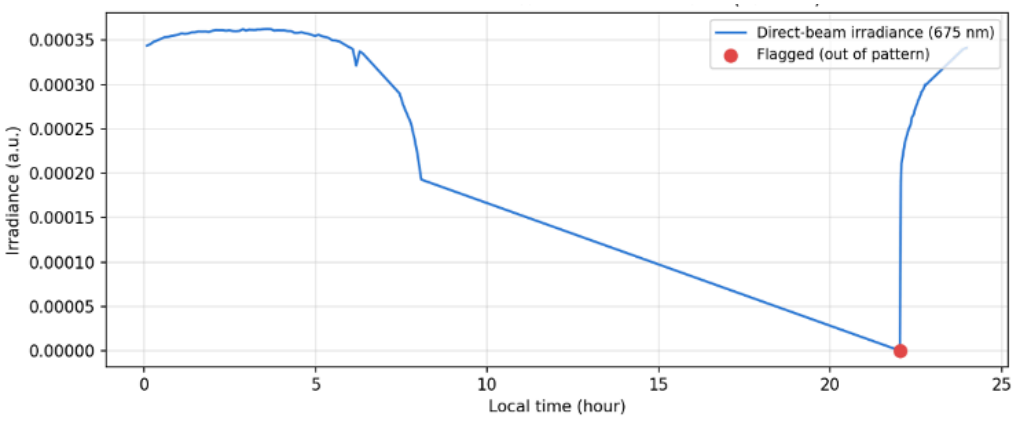


Figure 11 : Direct-beam smoothness check at 675 nm for 25Feb 2025

References

1. Kudo, R., Diémoz, H., Estellés, V., Campanelli, M., Momoi, M., Marenco, F., Ryder, C. L., Ijima, O., Uchiyama, A., Nakashima, K., Yamazaki, A., Nagasawa, R., Ohkawara, N., & Ishida, H. (2021). Optimal use of the Prede POM sky radiometer for aerosol, water vapor, and ozone retrievals. Atmospheric Measurement Techniques, 14(5), 3395–3426. https://doi.org/10.5194/amt-14-3395-2021
2. Momoi, M., Kudo, R., Aoki, K., Miura, K., & Nakajima, T. (2020). Development of on-site self-calibration and retrieval methods for sky-radiometer observations of precipitable water vapor. Atmospheric Measurement Techniques, 13(5), 2635–2658. https://doi.org/10.5194/amt-13-2635-2020
3. Nakajima, T., Hayasaka, T., Higurashi, A., Hashida, G., Moharram-Nejad, N., Najafi, Y., & Valavi, H. (1996). Aerosol optical properties in the Iranian region obtained by ground-based solar radiation measurements in the summer of 1991. Journal of Applied Meteorology, 35(8), 1265–1278. https://doi.org/10.1175/1520-0450(1996)035<1265:AOPITI>2.0.CO;2

4. Uchiyama, A., Matsunaga, T., & Yamazaki, A. (2018). The instrument constant of sky radiometers (POM-02) – Part 1: Calibration constant. Atmospheric Measurement Techniques, 11(9), 5363–5386. https://doi.org/10.5194/amt-11-5363-2018
5. Nakajima, T., Campanelli, M., Che, H., Estellés, V., Irie, H., Kim, S.-W., et al. (2020). An overview of and issues with sky radiometer technology and SKYNET. Atmospheric Measurement Techniques, 13, 4195–4218.
6. HARMONIA COST Action CA21119. Working Group 2: Improvement of aerosol products. https://www.cost.eu/actions/CA21119/
7. SKYNET International Data Center. About SKYNET. https://www.skynet-isdc.org/aboutSKYNET.php
8. EuroSkyRad (ESR). European SKYNET Radiometers network. https://www.euroskyrad.net/

6. HARMONIA activity for the ESA Validation Data Center (EVDC)

6.1 WORKFLOW OVERVIEW

The starting point for this activity was the consultation of the list of measurement campaigns considered within the Harmonia project. This list is included in the Harmonia deliverables D1.1 [R.2] and D2.1 [R.3], with additional details available in an Excel table shared among the Harmonia team (available on request).

Both these documents provide various pieces of information regarding the campaigns, the instruments involved, the derived and derivable products, and the acquisition modes (day/night).

Based on the campaign information, the first step was to compile a list of instruments and categorize them by type. Then, for each instrument, all associated products were then listed. Since not all this information is available in the Harmonia documents, it was obtained through targeted research on the instruments and, in some cases, with the support of the Principal Investigator (PI) of the measurement campaigns in which the instruments were used.

The diagram in Figure 1 outlines the sequential steps and key evaluation questions to be addressed, initially at the instrument level and subsequently at the product level.

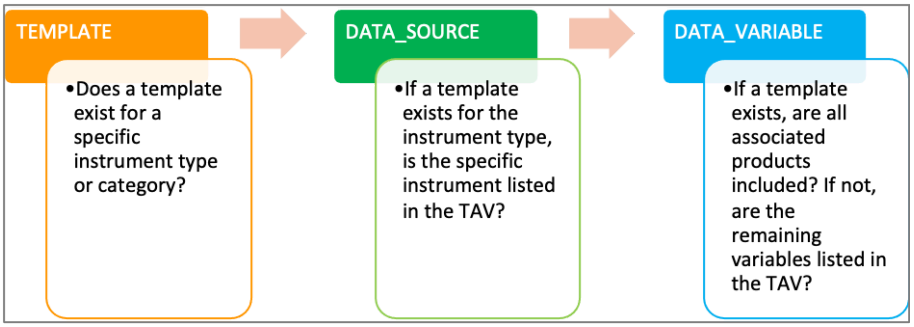


Figure 1 The diagram illustrates the main questions guiding the evaluation process, highlighting the logical steps and relationships between the different aspects analysed.

In the following two chapters, the instruments considered, and the measurable products will be listed. For each instrument and product, a brief description will be provided to highlight the available measurement methods (in the case of instruments) or the required ones (in the case of products, in order to derive the optical or physical properties of aerosols). Chapter four will offer an overview of the GEOMS format structure and its requirements, along with a description of the available templates for aerosol-related products. In the final chapter, all this information will be

brought together to identify the current availability and existing gaps in achieving GEOMS-compliant data formatting.

6.2. CLASSIFICATION OF INSTRUMENTS

The measurement campaigns considered by HARMONIA are twenty-four, in addition to these there are also twelve permanent monitoring stations.

The instruments involved can be classified into active and passive remote sensing instruments, in situ instrumentation, aircraft and sonde-based instruments. For the purposes of this activity, only instruments that allow the retrieval of aerosol-related products will be considerate. In addition, to easily look for a dedicated template, these instruments will be grouped into subcategories, as shown in Figure 2.

The subcategories identify the main characteristics of each instrument, both in terms of technology and measurement method; the parameters that can be derived from their measurements depend on both these aspects. Therefore, in the following sections, each instrument will be briefly described, and the respective aerosol parameters will be listed.

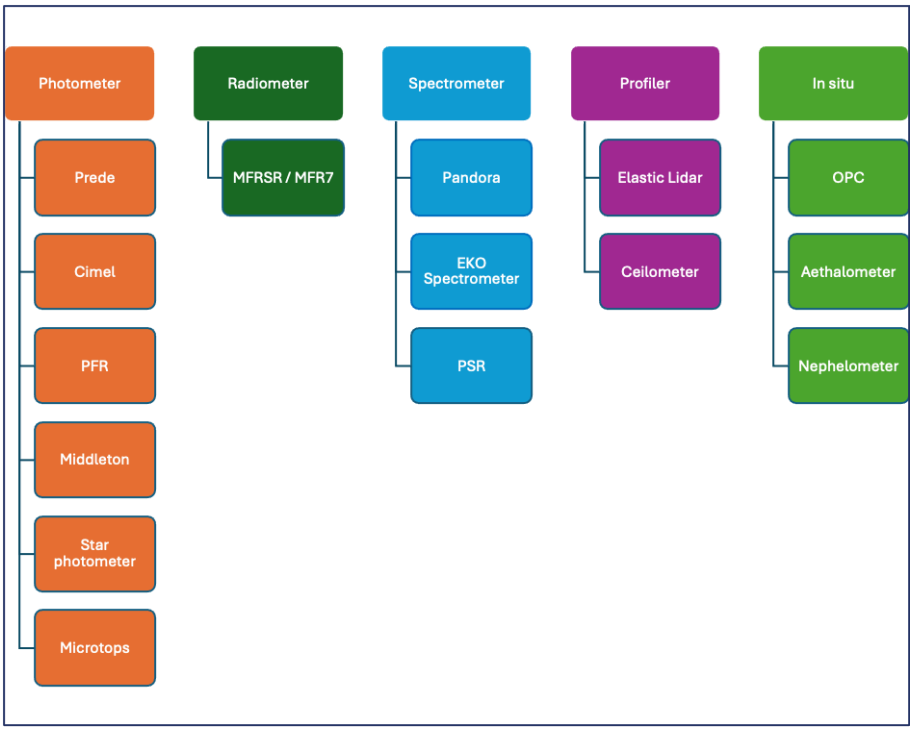


Figure 2 The figure illustrates the different categories analysed in the report and shows the specific instruments linked to each category.

The ***Prede POM and Cimel photometers*** are instruments equipped with a tracker capable of measuring direct radiation by pointing at the sun (some models can also track the moon), or at various azimuthal/zenithal angles. The sensors are equipped with filters for different wavelengths, which are mounted on a rotating filter wheel. With direct sun (or moon) measurements, the instruments can retrieve the Aerosol Optical Depth (AOD) for each wavelength, the Angstrom exponent (AE), and the water vapor column amount. The measurements taken out of sun direction (sky measurements) are used to retrieve other parameters as single scattering albedo (SSA), refractive index (RI), volume size distribution (VSD), asymmetry factor (AF), phase function (PF) and aerosol direct radiative forcing.

The ***PFR (Precision Filter Radiometer)*** is a reference photometric instrument used for measuring direct solar irradiance and AOD at four nominal wavelengths. It is designed to ensure high precision and long-term stability in atmospheric observations.

The ***Middleton Sun-photometer*** is a high-precision instrument designed for solar photometric measurements, primarily used for atmospheric aerosol characterization. It contains four narrowband spectro-pyrheliometers, each equipped with filters centred on specific wavelengths (typically in the visible and near-infrared range), allowing the retrieval of parameters such as, AOD, column ozone content, and water vapor content.

The ***star photometer*** is a passive remote sensing instrument designed to measure the spectral optical depth of the atmosphere by analysing attenuated starlight and to retrieve the AOD.

The ***Microtops sun-photometer*** is a portable, multispectral 5-channel instrument designed to measure AOD, direct solar irradiance, and column water vapor content. The instrument is lightweight, easy to operate in the field, and offers performance comparable to larger, more expensive instruments.

Both radiometers listed in **Error! Reference source not found.** belong to the ***Multifilter Rotating Shadow-band Radiometer (MFR)*** family, designed to measure spectral solar irradiance in its global, diffuse, and direct components. They use narrowband filters centred on specific wavelengths, plus one broadband channel. These instruments are used to derive AOD, ozone column content, and water vapor, and for radiative transfer studies.

The ***Pandora*** is a high-resolution ground-based spectrometer designed work in direct-Sun, zenith sky, and sky-scanning modes. It uses the Differential Optical Absorption Spectroscopy (DOAS) technique in to accurately retrieve total column and vertical profiles of atmospheric gases and aerosols. The AOD is one of the products under development for this instrument.

The ***EKO spectroradiometer*** is a compact, high-precision instrument designed for spectral direct solar irradiance measurements. It has been successfully used to retrieve AOD across multiple wavelengths, spectral range 340–870 nm.

The ***Precision Solar Spectroradiometer (PSR)*** is a high-resolution spectroradiometer developed by PMOD/WRC (Physikalisch-Meteorologisches Observatorium Davos / World Radiation Center) as an evolution of the PFR filter photometer. It is designed to measure direct spectral solar irradiance over a continuous wavelength range from 320 to 1040 nm, enabling the retrieval of AOD and atmospheric trace gases.

Both ***Elastic LIDAR*** (Light Detection and Ranging) and ***Ceilometer*** uses the same technology to analyse the vertical structure of the atmosphere, particularly the presence and distribution of aerosols and clouds. The Elastic Lidar uses laser pulses at one or more wavelengths (typically in the visible or UV range) and measures the backscattered radiation from atmospheric particles and provides high-resolution vertical profiles reaching altitudes of several tens of kilometres. The Ceilometer is a more compact and automated version of lidar, it uses infrared laser pulses (typically 905 or 1064 nm), has a shorter range than elastic lidar, but is ideal for continuous monitoring and operational use.

Optical Particle Counters (OPCs) are instruments that measure the number and size of aerosol particles suspended in the air. They work by passing particles through a laser beam and detecting the light scattered by each particle. The amount of scattered light is used to estimate the particle's size. OPCs are commonly used for monitoring air quality, measuring particulate matter (PM), and studying aerosol size distributions, typically for particles larger than about 0.3 µm.

Aethalometers are instruments used to measure the concentration of black carbon (BC) particles in the air. They work by drawing air through a filter and measuring the reduction in light transmitted through the filter as particles accumulate. The amount of light absorbed is directly related to the concentration of black carbon, which is an important component of atmospheric aerosols due to its effects on climate and air quality. Aethalometers provide real-time data and are widely used in environmental monitoring and research.

Nephelometers are instruments used to measure the amount of light scattered by aerosol particles suspended in the air. By detecting the intensity of scattered light at specific angles, nephelometers provide information about the concentration and optical properties of aerosols. These measurements are important for assessing air quality, visibility, and the impact of aerosols on climate.

6.3 AEROSOL PRODUCTS

Key aerosol parameters are essential for understanding their behaviour and their impact on climate, air quality, and health. These parameters are typically grouped into three categories: optical parameters describe how aerosols interact with light; physical parameters describe the size, shape, and distribution of aerosol particles; chemical parameters define the composition and reactivity of aerosols.

Table 1 Overview of aerosol products, including a brief description of each and an indication of whether it is obtained through direct or indirect measurement or derived via inversion techniques.

	Aerosol products	Descriptions
1	Aerosol Optical Depth (AOD)	AOD quantifies the amount of aerosol particles in a vertical column of the atmosphere. It is typically retrieved by measuring the attenuation of radiation at different wavelengths. To obtain accurate readings, instruments must be pointed directly at the sun (or the moon, for nighttime measurements).
2	Ångström Exponent (AE)	AE describes the wavelength dependence of aerosol optical depth (AOD) and provides information about the size distribution of aerosol particles. Since it is derived from AOD values at different wavelengths, it requires direct measurements of solar (or lunar) radiation.
3	Single Scattering Albedo (SSA)	SSA is the ratio of aerosol scattering to total extinction (scattering + absorption), and it indicates how efficiently aerosol particles scatter incoming radiation compared to how much they absorb. It is derived from direct and diffuse solar radiation measurements at multiple wavelengths.
4	Refractive Index (RI)	RI is a complex number describing how aerosol particles interact with light, combining both scattering (real part) and absorption properties (imaginary part). It is retrieved through inversion of multi-wavelength radiometric data, such as aerosol optical depth and sky radiance.
5	VSD	VSD describes how the volume of aerosol particles is distributed across different particle sizes. It is retrieved through inversion of multi-angle sky radiance measurements and spectral AOD data.
6	Asymmetry Factor (AF)	AF quantifies the average direction in which aerosol particles scatter incoming radiation. This parameter is not directly measured but is retrieved through inversion of multi-angle sky radiance measurements.
7	Phase Function (PF)	PF describes the angular distribution of scattered radiation by aerosol particles. It indicates how much light is scattered in different directions (forward, backward, or sideways) and is retrieved through inversion of multi-angle sky radiance measurements.
8	Backscatter ratio	Ratio between the total backscattered signal (aerosol + molecular) and the molecular backscatter alone. It provides insight into aerosol presence and intensity.
9	Backscatter coefficient (β)	Quantifies the amount of light scattered by aerosols in the backward direction per unit distance and per unit solid angle.

10	Extinction coefficient (α)	Measures the total attenuation of light due to aerosols, including both scattering and absorption, per unit distance.
11	Absorption Coefficient (σ)	Measure of how much light is absorbed by particles per unit distance as it passes through a medium. It quantifies the fraction of incident light that is absorbed by the particles in a given volume of air.
12	Lidar ratio	Ratio of the extinction coefficient to the backscatter coefficient. It is indicative of aerosol type and composition.
13	Depolarization ratio	Ratio of cross-polarized to co-polarized backscattered light in linear polarization.
14	Transmission	Represents the two-way transmission of the lidar signal through the atmosphere, accounting for attenuation during both upward and downward paths.
15	Particle Number Concentration (PNC)	Number of airborne particles present in a given volume of atmospheric air, obtained from in-situ in measurements.
16	Black Carbon concentration (BC)	Mass concentration of black carbon.

As previously mentioned, depending on the characteristics of the instrument and the measurement methods, each instrument may or may not be able to retrieve a specific type of product. Table 1 provides a list of aerosol products that can be retrieved from the instruments listed in , along with a brief description of each product. The aim is to highlight the diversity of aerosol parameters and the specific measurement requirements associated with their retrieval. Parameters numbered 8 to 13 can also be obtained through LIDAR-type observations. In this case, these variables describe the vertical distribution of aerosol optical properties in the atmosphere and will collectively be referred to as aerosol profiles.

Based on the instruments presented in Figure 2, and considering the information provided in the previous and current sections, Table 2 outlines the correspondence between each instrument and the aerosol products it can retrieve.

Table 2 Correspondence between aerosol products and the instruments capable of retrieving them, based on the measurement principles described in the text.

Types	**Instruments**	**Products**											
		AOD	**AE**	**SSA**	**RI**	**VSD**	**AF**	**PF**	**β**	**σ**	**BC**	**PNC**	**Aerosol profiles**
Photometer	Prede	X	X	X	X	X	X	X					
	Cimel	X	X		X	X	X	X					
	PFR	X	X										
	Middleton	X											

	Star photometer	X											
	Microtops	X											
Radiometer	MFRSR / MFR7	X											
Spectrometer	Pandora	X											
	EKO Spectrometer	X											
	PSR	X											
Profiler	Elastic Lidar	X	X										X
	Ceilometer	X	X										X
In situ	OPC											X	
	Aethalometer									X	X		
	Nephelometer								X				

6.4. GEOMS FORMAT

The GEOMS format was created to ensure that data files are consistent in both their content and their structure. This standardization makes it easier for users to understand and use the data.

GEOMS-format files include a set of attributes that provide various types of metadata, such as the instrument type, location, instrument principal investigator, data usage policy, and a description of the data itself. In addition, all the names of the variables included in the file must be formatted precisely according to GEOMS specifications and must include a set of attributes that enhance readability and interpretability. These attributes include, for example, product description, dimensions, units of measurement, and data type.

The values assigned to both global attributes and variable-specific attributes, as well as the variable names themselves, must conform to those listed in the TAV [R.6], which are continuously updated based on user requests and needs.

Particular attention must be paid to the naming of variables. Since variables may refer to the specific parameter, but also to its measurement mode or to additional information related to it (for example, the measurement uncertainty). It is possible to compose the variable name using three entries, so that the variable name appears as follows:

Variable name[_Variable mode][_Variable descriptor]

Of these, only the name entry is mandatory; the other two are optional. Furthermore, for each entry, the allowed options are those listed in the TAV, referring respectively to DATA_VARIABLE_01, DATA_VARIABLE_02, and DATA_VARIABLE_03 (for details, please refer to the documentation [R.5]).

On the EVDC webpage [R.4], several templates are also available, each devoted to a particular instrument (e.g. Photometers) or instrument/product pair (e.g. Lidar/aerosol). Each template includes a list of mandatory and optional variables, with the correct variable names formatted according to GEOMS standards, along with the corresponding descriptions, units, data types, dimensions, and dependencies between variables.

The list of templates [R.7], as well as the templates themselves, are continuously updated. Currently, 41 templates are available; however, in the context of this activity, the focus is only on those templates related to aerosol products. The reference templates relevant to this report are listed below. The order in which they are presented follows the sequence established in the previous classification of the instruments.

- GEOMS-TE-PHOTOMETER-001
- GEOMS-TE-LIDAR-AEROSOL-006
- GEOMS-TE-LIDAR-AEROSOL-L3-001
- GEOMS-TE-OPC-AEROSOL-001
- GEOMS-TE-NEPHELOMETER-001

An individual examination of each template will now be conducted, with the objective of identifying their principal characteristics, assessing their potential applications, and highlighting any associated limitations or critical aspects. In what follows, all mandatory variables will be considered. However, variables such as ALTITUDE.INSTRUMENT, LATITUDE.INSTRUMENT and LONGITUDE.INSTRUMENT, which are common to all templates and do not provide meaningful contributions to the current discussion, will henceforth be excluded from further mention.

6.4.1. GEOMS-TE-PHOTOMETER-001

As indicated by its title, this template is specifically intended for instruments belonging to the photometer category. The two variables related to aerosol properties are AEROSOL.OPTICAL.DEPTH and AEROSOL.ANGSTROM.EXPONENT.

The AEROSOL.OPTICAL.DEPTH variable is two-dimensional: the first dimension is associated with the DATETIME variable, which specifies the date and time of the measurement, while the second dimension is linked to the WAVELENGTH variable, which indicates the wavelength considered.

Similarly, the AEROSOL.ANGSTROM.EXPONENT variable is also two-dimensional, with DATETIME as one dimension, and as the second one AEROSOL.ANGSTROM.EXPONENT_WAVELENGTH.INDEX. The

latter, together with the AEROSOL.ANGSTROM.EXPONENT_WAVELENGTH.PAIR variable, allows identification of the two wavelengths used in the retrieval.

Other variables present in the template are ANGLE.SOLAR_ZENITH.ASTRONOMICAL and AIR.MASS, which indicate the possibility of using this template for direct solar radiation measurements. The last mandatory variable is the instrument's internal temperature, INTERNAL.INSTRUMENT.TEMPERATURE, which serves as an indicator of the instrument's operational stability.

No additional aerosol variables, such as those that may be among the products of photometers, as shown in the table, are included in this template. Furthermore, there is no provision for including AOD and AE values derived from lunar measurements, as there is no variable available for recording the lunar azimuth angle.

6.4.2. GEOMS-TE-LIDAR-AEROSOL-006

This template is specifically designed for a particular instrument, the elastic lidar, and most of the variables associated with aerosol parameters are optional, facilitating the adaptation of the format to systems with several characteristics and capabilities, while still establishing a standard for variable naming and definition. Here, the description begins with the mandatory variables.

The timing of the measurement is indicated by the variables DATETIME.START and DATETIME.STOP, which represent the start and end of the measurement period, respectively, while DATETIME denotes the central value of this time interval.

The variables WAVELENGTH_EMISSION and WAVELENGTH_DETECTION, as suggested by their names, refer to the laser emission and system reception wavelengths. These variables may be multidimensional, which is particularly useful in the case of multi-wavelength lidar systems.

The zenith angle at which the lidar is pointed, and optionally the azimuth angle if the pointing mode is not vertical, are represented by ANGLE.VIEW_ZENITH and ANGLE.VIEW_AZIMUTH variables, respectively. Both variables may be constant or dependent on DATETIME or the emitted wavelength, depending on the system configuration. Finally, the variable ALTITUDE reports the altitude at which the measurement is performed.

The variables MOLECULAR.BACKSCATTER.COEFFICIENT_INDEPENDENT, representing the computed molecular profile used in the retrieval process, and MOLECULAR.BACKSCATTER.COEFFICIENT_INDEPENDENT_SOURCE, describing its origin, are the last two mandatory variables.

As previously mentioned, all other variables contained in the template are optional. However, the inclusion of any of these variables requires the simultaneous inclusion of additional related variables, which provide important contextual information linked to the parameter in question. To simplify reading, the Table 3 presents the values of the two fields, VARIABLE_01 and VARIABLE_02, which together constitute the variable name. To clarify, if one intends to include a variable from the first column, it is necessary to also include all variables whose names are formed by combining that variable with each of those listed in the second column.

Table 3 The table reports the values of the two fields, VARIABLE_01 and VARIABLE_02, which together constitute the variable name of the optional variables included in template GEOMS-TE-LIDAR-AEROSOL-006.

DATA_VARIABLE_01	DATA_VARIABLE_03
AEROSOL.BACKSCATTER.RATIO	UNCERTAINTY.COMBINED.STANDARD
AEROSOL.BACKSCATTER.COEFFICIENT	UNCERTAINTY.RANDOM.STANDARD
AEROSOL.BACKSCATTER.COEFFICIENT	UNCERTAINTY.SYSTEMATIC.STANDARD
AEROSOL.BACKSCATTER.COEFFICIENT.CIRCULAR	RESOLUTION.ALTITUDE
AEROSOL.LIDAR.RATIO	INTEGRATION.TIME
AEROSOL.LIDAR.RATIO.CIRCULAR	RETRIEVAL.METHOD
AEROSOL.ANGSTROM.EXPONENT	
AEROSOL.DEPOLARIZATION.RATIO.LINEAR	
AEROSOL.DEPOLARIZATION.RATIO.CIRCULAR	
AEROSOL.TRANSMISSION.TWOWAY	
VOLUME.DEPOLARIZATION.RATIO.LINEAR	
VOLUME.DEPOLARIZATION.RATIO.LINEAR	
VOLUME.DEPOLARIZATION.RATIO.CIRCULAR	
AEROSOL.LAYER.BASE.HEIGHT	
AEROSOL.LAYER.TOP.HEIGHT	

6.4.3. GEOMS-TE-LIDAR-AEROSOL-L3-001

This template is also dedicated to elastic lidar and is very similar to the previous one. There are some differences in the list of variables, here they are fewer, and in the additional information associated with them. The mandatory variables are the same as those listed for the previous template. As in the previous case, to simplify reading, the entries which compose the name of the variables, are listed in a Table 4.

Table 4 The table reports the values of the two fields, VARIABLE_01 and VARIABLE_02, which together constitute the variable name of the optional variables included in template GEOMS-TE-LIDAR-AEROSOL-L3-001.

DATA_VARIABLE_01	DATA_VARIABLE_03
AEROSOL.BACKSCATTER.RATIO	MEAN
AEROSOL.BACKSCATTER.COEFFICIENT	MEAN.STANDARD
AEROSOL.EXTINCTION.COEFFICIENT	MEDIAN
AEROSOL.LIDAR.RATIO	UNCERTAINTY.COMBINED.STANDARD

AEROSOL.ANGSTROM.EXPONENT	COUNT
AEROSOL.LINEAR.DEPOLARIZATION.RATIO	RESOLUTION.ALTITUDE [1]
VOLUME.LINEAR.DEPOLARIZATION.RATIO	INTEGRATION.TIME
AEROSOL.LAYER.BASE.HEIGHT [2]	RETRIEVAL.METHOD [3]
AEROSOL.LAYER.TOP.HEIGHT **3**	
MIXING.LAYER.BASE.HEIGHT **3**	
MIXING.LAYER.TOP.HEIGHT **3**	

6.4.4. GEOMS-TE-OPC-AEROSOL-001

This template is designed for OPCs and includes a single aerosol-related variable: AEROSOL.NUMBER.DENSITY, which represents the particle number concentration. To define this variable correctly, three other variables are needed: DATETIME, which provides the timestamp of the measurement, PARTICLE.SIZE, which indicates the average particle size for each bin, and PARTICLE.SIZE.BOUNDARIES, which defines the lower and upper size limits for each bin.

In addition to these, the template includes a mandatory variable, AEROSOL.NUMBER.DENSITY_UNCERTAINTY.COMBINED.STANDARD, which gives the uncertainty estimate of the number concentration for each size bin, and an optional variable, AEROSOL.NUMBER.DENSITY_FLAG, used to indicate the data quality of the measurement.

6.4.5. GEOMS-TE-NEPHELOMETER-001

This template refers to nephelometers, and the variable related to aerosols is AEROSOL.BACKSCATTER.COEFFICIENT, where it is possible to enter the values of the aerosol backscattering coefficient obtained at different wavelengths, specified in the WAVELENGTH variable, and for each measurement performed by the instrument (DATETIME is the time variable). There is also the TOTAL.SCATTERING.COEFFICIENT variable, which refers to the total backscattering parameter, with the same dependencies as the previous one.

The other mandatory variables provide information about the integration time of the measurement (INTEGRATION.TIME) and the conditions under which it is performed, specifically the temperature, pressure, and humidity measured inside the instrument; these parameters are associated with the

variables INTERNAL.INSTRUMENT.TEMPERATURE, INTERNAL.INSTRUMENT.PRESSURE and INTERNAL.INSTRUMENT.HUMIDITY.RELATIVE. The template also includes additional mandatory variables where information on measurement quality can be provided in the form of flags (see the appendix for further details).

Even though the name of the template is GEOMS-TE-NEPHELOMETER, without specifying the type or model of the instrument, reading the descriptions of variables AEROSOL.BACKSCATTER.COEFFICIENT and TOTAL.BACKSCATTER.COEFFICIENT, there is a reference to a specific instrument, the TSI 3563 Nephelometer. Similarly, in the description of the variable WAVELENGTH, the same wavelengths are specified. Such detailed and specific descriptions of the variables might suggest that the template is dedicated to this specific instrument.

6.5. INTEGRATION OF INSTRUMENTS, PRODUCTS, AND TEMPLATES: AVAILABILITY AND GAPS

Having described the available instruments, the corresponding retrievable products, and the set of GEOMS templates, this section brings these elements together. Specifically, we analyse the association between each instrument and its related products and verify whether a suitable GEOMS template exists for each case. This analysis provides a comprehensive overview of the current coverage of GEOMS templates with respect to the instrument–product associations considered in this study and helps to identify any gaps that may require future development or adaptation of templates.

The steps for this activity, as well as the key questions to be addressed at this stage, are illustrated in the diagram shown. As a starting point for this assessment, reference is made to Table 2, in particular to the first two columns, which specify the type and the instrument. In order to enhance the clarity of the information presented, the cells of this table have been reproduced in a revised, color-coded format in Table 5 and the significance of each colour is detailed in the accompanying legend Table 6.

Table 5 Correspondence between aerosol products and the instruments capable of retrieving them as in Table 2. Here, the coloured cells help to indicate the availability of templates, as well as the presence of instruments and products within the TAVs. For the colour legend, please refer to the Table 6.

Types	Instruments	Products											
		AOD	AE	SSA	RI	VSD	AF	PF	β	α	BC	PNC	Aerosol profiles
Photometer	Prede	X	X	X	X	X	X	X					
	Cimel	X	X		X	X	X	X					
	PFR	X	X										
	Middleton	X											
	Star photometer	X											
	Microtops	X											
Radiometer	MFRSR / MFR7	X											
Spectrometer	Pandora	X											
	EKO Spectrometer	X											
	PSR	X											
Profiler	Elastic Lidar	X	X										X
	Ceilometer	X	X										X
In situ	OPC											X	
	Aethalometer									X	X		
	Nephelometer								X				

Table 6 This table show the meaning of the colours used in the Table 5.

Template available for the instrument type or for a specific instrument
DATA_SOURCE or DATA_VARIABLE defined for a specific instrument or product
Template, DATA_SOURCE, or DATA_VARIABLE not available
DATA_VARIABLE is available and, if a template exists, it is included in the template
DATA_VARIABLE is available but, if a template exists, it is not included in the template
DATA_VARIABLE not available

In this table, there are five types of instruments listed, but only one of them, the photometer, has a dedicated template GEOMS-TE-PHOTOMETER-001 [A14.1].

However, if we also consider the second column, which lists the specific instruments, it is possible to use templates for other instruments. For the Elastic Lidar there are two option GEOMS-TE-LIDAR-AEROSOL-006 [A2] and GEOMS-TE-LIDAR-AEROSOL-L3-001 [A3], the selection of the appropriate template depends on which variables are intended or technically feasible to include in the file. This is determined by the specific characteristics and measurement capabilities of the instrument in question. For the OPC and Nephelometer the dedicated templates are respectively GEOMS-TE-OPC-AEROSOL-001 [A4] and GEOMS-TE-NEPHELOMETER-001 [A5].

By cross-referencing the list of instruments with the possible options for the DATA_SOURCE field defined in the GEOMS format, it becomes evident that only six valid correspondences exist. Specifically, these are:

- PHOTOMETER.CIMEL
- PHOTOMETER.PREDE
- LIDAR.AEROSOL
- CEILOMETER.AEROSOL
- OPC.AEROSOL
- NEPHELOMETER

Regarding the products, as indicated in the Table 5, the majority already have a corresponding DATA_VARIABLE defined. For the remaining products, however, an appropriate DATA_VARIABLE still needs to be established. Below, all products are listed together with their corresponding entries, apart from those belonging to Aerosol profiles, for which reference should be made to Table 1 and Table 5.

- AOD → AEROSOL.OPTICAL.DEPTH
- AE → AEROSOL.ANGSTROM.EXPONENT
- SSA → AEROSOL.SINGLE.SCATTERING.ALBEDO
- AF → AEROSOL.ASYMMETRY.FACTOR
- β → BACKSCATTERING.COEFFICIENT
- σ → ABSORPTION.COEFFICIENT
- PNC → AEROSOL.NUMBER.DENSITY

Products β and σ in the table are associated exclusively with instrument Aethalometer, which is primarily used to measure black carbon properties. The corresponding DATA_VARIABLE entries indicated here are generic, meaning that they do not specify whether the measurement refers to aerosols or other substances. Should a dedicated template be developed for this instrument in the

future, it is possible that these variables could be defined in a more specific manner, and in line with the approach adopted for other variables, the options could, be BC.BACKSCATTERING.COEFFICIENT and BC.ABSORPTION.COEFFICIENT.

The Table 5 provides a comprehensive overview of the status and enables a series of technical considerations regarding existing data gaps.

Each of the instruments listed, both ground-based and in-situ, provides products of significant value for calibration and validation activities and beyond. Facilitating the sharing and access to these data within the EVDC user community would be highly advantageous. Furthermore, these instruments are widely deployed, and their inclusion would contribute to the establishment of a substantial and unquestionably valuable data repository. It is therefore recommended to introduce specific entries for these instruments among the permissible values of the DATA_SOURCE attribute.

A more detailed examination of the information in Table 5 allows for additional observations and comments.

The photometer template [A1] is generally applicable to all instruments of this type, although certain modifications are required (further details are provided later in the text). The only potential exception is represented by Star photometers, which measure radiation originating from stellar sources. The current template is incompatible with these instruments due to the mandatory ANGLE.SOLAR_ZENITH.ASTRONOMICAL variable (as specified in 4.1), which is not relevant in this context. It would thus be necessary to define two new variables representing the zenith and azimuth observation angles, or alternatively, to develop a dedicated template for this specific instrument.

Similarly, MFRSR radiometers and their updated version, MFR7, could utilize a template analogous to that of photometers, potentially excluding products related to sky measurements (which are not performed by these instruments), but including the optional variables H2O.COLUMN_ABSORPTION.SOLAR and O3.COLUMN_ABSORPTION.SOLAR, as they are a derivable products. Additionally, variables associated with direct and diffuse global radiation measurements for specific wavelengths and broadband, as measured by the instrument, could be included. It should be noted that a dedicated template for radiometers already exists, GEOMS-TE-RADIOMETER-BROADBAND-001, and several of the required variables are already defined (refer to A6 for further details).

Regarding spectrometers, starting with Pandora, and by analogy with the existing templates dedicated to measurement type for gases, it would be appropriate to develop a specific template for aerosol products, as well as a corresponding value for the DATA_SOURCE attribute, such as PANDORA.AEROSOL (given the existence of entries such as PANDORA.O3 and PANDORA.NO2). In

any case, as previously stated, these products are currently under development, and it would be prudent to wait before assessing which aerosol-related parameters can be reliably retrieved from Pandora measurements.

Although templates already exist for spectrometers, they are primarily designed for gas products. A unified template for aerosol products could be developed, taking into account the specific measurement and retrieval techniques used by these instruments.

As previously discussed, two templates are available for lidar instruments; however, neither includes the AEROSOL.OPTICAL.DEPTH variable, except as an independent variable in the GEOMS-TE-LIDAR-AEROSOL-006 template. At present, no template exists for ceilometers, which can provide both aerosol and cloud products; all such products could be incorporated into a single template. It should be noted, however, that two options currently exist for the DATA_SOURCE attribute for this instrument: CEILOMETER.AEROSOL and CEILOMETER.CLOUD, which would not be applicable in the case of a unified template.

Finally, among the listed in-situ instruments, only the Aethalometer lacks a defined template. Given the specificity of this instrument, particularly its focus on black carbon (BC), and the considerable importance of this product, it would be advisable to consider the development of a dedicated template.

Focusing on the photometer template, it is useful to carefully examine the variables it contains to assess its applicability to all the instruments listed. This template includes several mandatory variables, but not all these variables can be derived from other instruments within the same category. For instance, the AAE product cannot be retrieved from the Middleton, Star photometer, or Microtops instruments. To ensure template applicability across these cases, it would be necessary to revise the template by making the AEROSOL.ANGSTROM.EXPONENT variable, and its dependent variables AEROSOL.ANGSTROM.EXPONENT_WAVELENGTH.INDEX and AEROSOL.ANGSTROM.EXPONENT_WAVELENGTH.PAIR, optional.

Additional derived products, such as SA, RI, VSD, AF, and PF, cannot be obtained from all photometers. Therefore, it would be advisable to define the associated variables as optional within the template to accommodate these limitations.

Another important aspect concerns the two distinct measurement modalities supported by photometers:

- Direct measurements, performed by targeting the sun or moon.
- Indirect measurements, conducted by observing at various zenith and azimuth angles.

These modalities are executed at different times, implying that the derived parameters will have distinct timestamps. Specifically, direct measurements yield AOD and AE, whereas RI, VSD, AF, and PF are obtained from indirect measurements. The timestamp is recorded in the DATETIME variable, for this variable, if the value corresponds to a direct measurement, AEROSOL.OPTICAL.DEPTH and AEROSOL.ANGSTROM.EXPONENT should be populated, while the remaining variables should be assigned a fill value. Conversely, for indirect measurements, the roles are reversed.

To improve clarity regarding the measurement type and enhance file interpretability, it would be beneficial to introduce a new variable containing a flag to explicitly indicate the measurement modality. An alternative approach would be to implement a dual-template system, like what is done for other instruments such as Pandora, which uses:

- GEOMS-TE-PANDORA-DIRECTSUN-GAS-003
- GEOMS-TE-PANDORA-OFFAXIS-GAS-001

The single-template approach offers the advantage of consolidating all parameters into one file, simplifying data management. However, this comes at the cost of increased file size and a high number of fill value entries. The dual-template solution, on the other hand, results in smaller and likely more readable files, but has the drawback of doubling the number of files required per instrument.

Further considerations pertain to lunar measurements: the existing template cannot be used due to the mandatory ANGLE.SOLAR_ZENITH.ASTRONOMICAL variable. A new variable, ANGLE.LUNAR_ZENITH.ASTRONOMICAL, would be required, and both should be optional. Referring to the two previously proposed approaches (single vs. dual template):

- In the single-template scenario, the ANGLE.LUNAR_ZENITH.ASTRONOMICAL variable should be added, along with an additional flag value to distinguish lunar measurements.
- In the dual-template scenario, lunar measurements should be included only in the template for direct measurements. In both cases, the inclusion of ANGLE.LUNAR_ZENITH.ASTRONOMICAL and a flag to differentiate between solar and lunar direct measurements would be useful.

6.6. REFERENCES

R.1 HARMONIA COST Action: https://harmonia-cost.eu/

R.2 HARMONIA Deliverable 1.1, Create a list of existing and foreseen campaigns or experiments needed for night and day aerosol measurements and report on the data collection and analysis of the data/measurements:

https://harmonia-cost.eu/wp-content/uploads/2023/10/COST_CA21119_HARMONIA-WG1_Deliverable-D11.pdf

R.3 HARMONIA Deliverable 2.1, Report on synergistic approaches towards better quality products: https://harmonia-cost.eu/wp-content/uploads/2023/10/Harmonia_D21_v2.pdf

R.4 EVDC: https://evdc.esa.int/

R.5 GEOMS: https://evdc.esa.int/documentation/geoms/

R.6 Table of Attributes Value version: tableattrvalue_04R101.dat https://git.nilu.no/geoms/documentation/blob/master/tableattrvalue_04R101.dat

R.7 Templates list: https://evdc.esa.int/tools/data-formatting-templates/

---

[1] Required for all variables except AEROSOL.ANGSTROM.EXPONENT

[2] These variables require as additional information only MEAN, MEAN.STANDARD and MEDIAN

[3] Required for all variables except AEROSOL.LINEAR.DEPOLARIZATION.RATIO and VOLUME.LINEAR.DEPOLARIZATION.RATIO